universität wien

MASTERARBEIT / MASTER'S THESIS

Titel der Masterarbeit / Title of the Master's Thesis

„Contributions to the mineralogy of the Lavrion mining district, Greece"

verfasst von / submitted by

Irene Liebhart, BSc

angestrebter akademischer Grad / in partial fulfilment of the requirements for the degree of

Master of Science (MSc)

Wien, 2023 / Vienna, 2023

Studienkennzahl lt. Studienblatt / degree programme code as it appears on the student record sheet:	UA 066 815
Studienrichtung lt. Studienblatt / degree programme as it appears on the student record sheet:	Masterstudium Erdwissenschaften
Betreut von / Supervisor:	Ao. Univ.-Prof. Mag. Dr. Gerald Giester

Table of Contents

1. Acknowledgements 1
2. Introduction 2
2.1 Regional geology 4
2.2 Geology of the Lavrion area 5
2.3 Types of mineralization 6
2.3.a Porphyry type (Mo-W) 7
2.3.b Skarn type (Fe-Cu-Bi-Au-Te) 7
2.3.c Carbonate-replacement mineralization (Pb-Zn-Cu-Ag-Au, skarn-free) 7
2.3.d,e Pb-Zn-Ag-Au epithermal veins and breccias 8
2.4 Historical 8
2.5 Type locality 8
2.6 Objectives 9
3. Methods 10
3.1 Single-crystal X-ray diffraction 10
3.2 Raman spectroscopy 10
3.3 Infrared spectroscopy 10
3.4 Chemical analysis 11
4. Guérinite 12
4.1 Results 13
4.2 Discussion 21
5. Bismoclite 26
5.1 Results 26
5.2 Discussion 29
6. Tzeferisite 32
6.1 Results 33
6.2 Discussion 38
7. Conclusion 42
8. List of Figures and Tables 43
9. References 45
10. Appendix 54
Abstract (english) 58
Abstract (deutsch) 59

1. Acknowledgements

Many thanks to my supervisor Gerald Giester, who always took his time and supported me in completing my Master's thesis on time. I would also like to thank Branko Rieck, who provided me with his collected minerals from the Lavrion area, and my work colleagues at the Institute of Mineralogy and Crystallography for the acquisition time: Manuela Zeug and Chutimun Changmuang Nasdala at the Raman spectroscope and Eugen Libowitzky at the infrared spectroscope. Lutz Nasdala for his help in analysing the Raman data and providing old, non-digital papers. Michi Neuwirth, who always motivated me to finish my work. My parents Lucia and Hans, who I can always count on. Finally, I would like to thank my husband Christian because I could concentrate on my education without worries.

2. Introduction

The Lavrion mining district is situated in the southeast part of the Attika peninsula, Greece. The mining area extends around 150 km^2 divided into several districts (e.g. Kamariza, Plaka, Lavrion). Athens, the capital of Greece, is located 50 km northwest of the Lavrion mining district (Figure 1). The Lavrion stratigraphy is believed to have formed about 5 million years ago by tectonic uplift associated with variations in paleoclimate (Voudouris et al., 2021).

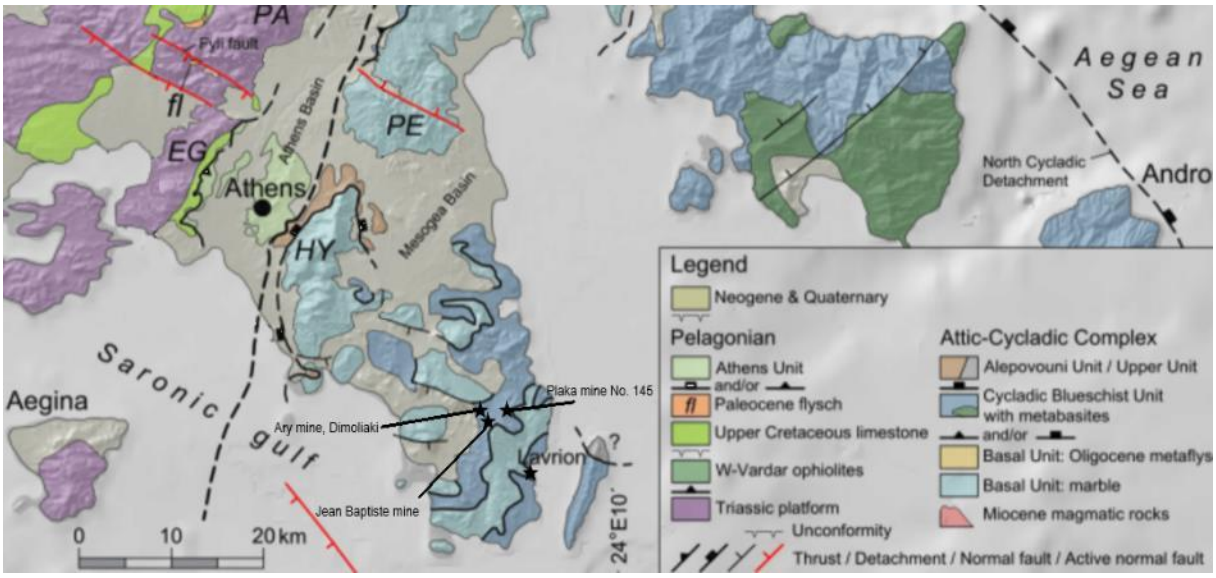

Figure 1. Geological map of Attica, Greece (Boronkay et al., 2021 created with www.geomappapp.org).

The sample material for my studies was provided by mineralogist Branko Rieck (B.R.), Austria, who has been travelling to the Lavrion area for decades, exploring, surveying and investigating the old mines and new outcrops. He regularly brings back new sample material from his excursions leading to the discovery of new mineral species (Rieck, B. 2012; Rieck et al., 2018; Rieck et al., 2020c; Rieck et al., 2022).

Guérinite $Ca_6(HAsO_4)_3(AsO_4)_2 \cdot 10.5H_2O$ (Figure 2) was collected from a banded, vein-type mineralization from the Plaka mine No. 145 on 12th April 2019. The veins known as “vein 80” or “Filoni 80” are up to two meters wide and extend 1 km from East to West between Plaka and Adami Valley (Conophagos, 1980; Skarpelis, 2007; Voudouris, et al., 2008). Alteration of hydrothermal hornfels and skarnoids are rich in Pb-As-Sb-Zn-Cu-Ag sourced from a contact metamorphic zone. The mineralogy of the oxidation zone comprises rauenthalite, marcasite, pharmacolite, arsenopyrite, chalcopyrite, sphalerite, pyrite, calcite, fluorite, quartz (Rieck, B. & Rieck, P. 1999; Wendel et al., 1999a; Wendel et al., 1999b; Skarpelis 2007; Voudouris et al., 2008; Rieck et al., 2018).

Agios Konstantinos is located in the northwestern part of Lavrion mining area, were B.R. found bismoclite BiOCl in the Jean Baptiste mine on 26th April 2014 (Figure 3). The small mine is connected by shafts to a more profitable winding shaft of the Serpieri mine. The few stockpiles indicate a low economic outcome from mining. The Jean Baptiste shaft is known as a locality for adamine $Zn_2(AsO_4)(OH)$ and carminate $PbFe^{3+}{}_2(AsO_4)_2(OH)_2$.

Tzeferisite $CaZn_8(SO_4)_2(OH)_{12}Cl_2 \cdot 9H_2O$ (Figure 4), identified as a new mineral species (IMA no. 2022-094) (Rieck et al., 2023), was collected from the small Ary mine in Dimoliaki on 2nd November 2021. The Ary mine is characterized by a carbonate-replacement Pb-Zn-Ag

mineralization (Skarpelis, 2007; Voudouris et al., 2008a,b; Skarpelis & Argyraki, 2009; Bonsall et al., 2011; Voudouris et al., 2021). In the ore-poor mine, tzeferisite is associated with sphalerite, galena, greenockite, hemimorphite, gypsum, calcite and dolomite.

Figure 2. Detail of the Plaka mine where guérinite was discovered in April 2019. © Branko Rieck

Figure 3. Locality of bismoclite in the Jean Baptiste mine, April 2014. © Branko Rieck

Figure 4. Spot of tzeferisite in the Ary mine, November 2021. © Branko Rieck

2.1 Regional geology

The Lavrion mining district is part of the Attic-Cycladic crystalline belt in the central Aegean region. This polymetamorphic zone is located within the Hellenides, a part of the Alpine mountain formation (Papanikolaou, 1987; Jolivet et al., 2010; Ring et al., 2010; Jolivet et al., 2013). They were formed in the late Jurassic at an active subduction zone when the African plate subducted under the European plate (Papanikolaou, 1987; Photiades & Carras, 2001; Bröcker et al., 2004; Forster & Lister, 2005; Bröcker & Keasling, 2006). Since the Cretaceous, there has been a steady plate shift back towards the South Aegean. The post-orogenic extension of the Aegean Back-Arc basin led to the exhumation of metamorphic cores from the crust (Lister et al., 1984; Gautier & Brun, 1994; Avigad et al., 1997; Jolivet et al., 2003; Ring & Layer, 2003; Jolivet et al., 2013). The Attic-Cycladic crystalline belt is divided into three tectonic units from bottom to top: the Cycladic basement or basal unit, the Cycladic blueschist unit and the Upper tectonic unit. The Cycladic basement consists of pre-Carboniferous schists and Carboniferous gneisses, not exposed in the Lavrion area (Papanikolaou, 1987; Bröcker et al., 2004; Forster & Lister, 2005; Ring et al., 2010; Jolivet et al., 2013; Seman et al., 2017; Wind et al., 2020). The Cycladic blueschist unit includes metapelites, marbles, meta-vulcanites, calc-silicate schists and Permo-Carboniferous meta-igneous rocks from the Mesozoic era. The Cycladic blueschist unit underwent three phases of metamorphism in the Tertiary (56 – 5 mya). First, a blueschist to eclogite facies metamorphism initiated during Eocene subduction. In the second phase, metamorphism resulting in the upper greenschist facies and synorogenic exhumation occurred (Oligocene). The third phase was the consequence of the plate retrogression process and initiated an

orogenic collapse, opening the Aegean back-arc basin and allowing the post-orogenic exhumation of the crust in the form of metamorphic core complexes, green-shale to upper amphibolite metamorphism in Miocene. It was followed by crustal anataxis and exhumation of the Attic-Cycladic metamorphic complex about 17 Ma ago. This extension event allowed intrusion of various granitoids throughout the Attic-Cycladic belt in the late Miocene (Kruckenberg et al., 2011; Jolivet et al., 2013; Grasemann et al., 2018; Coleman et al., 2020).
The Upper tectonic unit consists of various sequences of Upper Permian to Jurassic volcanoclastics, ophiolites and carbonates, Cretaceous to Tertiary greenschist rocks and late Cretaceous amphibolite rocks and granitoids. This unit shows the lowest grade of metamorphism (Reinecke et al., 1982; Jolivet et al., 2010; Grasemann et al., 2012; Ring et al., 2010).

2.2 Geology of the Lavrion area

The Lavrion area is located on the western boundary of the Attic-Cycladic crystalline belt. The area consists of three main tectonic units of Alpine age: the Kamariza or Lower tectonic unit, the Lavrion blueschist or Middle tectonic unit and the Berzekos or Upper tectonic unit (Photiades & Carras, 2001; Lekkas et al., 2011; Seman et al., 2017; Coleman et al., 2019). The lowest unit underwent three stages of deformation and metamorphism: syn-orogenic burial during subduction, syn-orogenic exhumation in the Oligocene under greenschist facies conditions and post-orogenic exhumation in the Miocene by related movements a detachment system (Reinecke et al., 1982; Scheffer et al., 2016; Coleman et al., 2019; Tarantola et al., 2021).
The Kamariza unit consists of Late Triassic and pre-Jurassic marble and Kamariza schist. The 300 m massive Kamariza schist is surrounded by folded lower and upper marble (150 m and up to 500 m thick, respectively). The Kamariza unit is characterized by syn-orogenic blueschist-facies metamorphism overprinting by pre-Miocene greenschist facies metamorphism during post-orogenic exhumation. It occurred under ductile conditions up to late Miocene and under brittle conditions in late Miocene (Marinos & Petrascheck, 1956; Leleu & Neumann, 1969; Katsikatsos, 1977; Marinos et al., 1977; Katsikatsos et al., 1986; Photiades & Carra, 2001; Photiades, 2003; Lekkas et al., 2011; Berger et al., 2013; Seman et al., 2013; Coleman et al., 2019).
The Lavrion blueschist unit consists of upper and lower marble and Lavrion schist with lenses of metabasic rocks from the Late Jurassic to Cretaceous. It is characterized by Eocene blueschist-facies metamorphosis followed by Oligocene greenschist-facies metamorphosis during syn-orogenic exhumation, which brittle conditions in the middle Miocene (~14 Ma), while the Kamariza unit was ductile deformed. (Marakis, 1968; Reinecke et al., 1982; Baltatzis, 1996; Photiades & Carras, 2001; Lekkas et al., 2011; Seman et al., 2013; Seman et al., 2017; Coleman et al., 2019.)
The 80 m thick Berzekos unit is characterized by non-metamorphic limestone from the upper Cretaceous. It contains chert, serpentinite and non-metamorphic limestone. The upper tectonic unit is not well exposed in the Lavrion mining district (Photiades & Carras, 2001; Photiades & Saccani, 2006; Lekkas et al., 2011).

The exposed West Cycladic detachment system (Figure 5) in the Lavrion area has a dominantly ductile to brittle sub horizontal detachment zone (Grasemann et al., 2012; Coleman et al., 2019). The mylonitic to ultramylonitic marble and schist shown at the footwall transitions structurally in the hanging wall under a cataclastic fault in the marble and schist (Lekkas et al., 2011; Scheffer et al., 2016; Coleman et al., 2019). The detachment fault consists of several meters of ultramylonitic upper Kamariza marble and is overlain by a cataclastic mélange (up to 4 m thick) (Lekkas et al., 2011; Ross et al., 2021). Both the marble and the Kamariza schist were initially ductile deformed and was later transformed into cataclastic to brittle material. The Plaka area was intruded by a Late Miocene granodiorite stock (Altherr et al., 1982) in the footwall. The prominent granodiorite crosscuts the metamorphic footwall rocks in the Plaka area and generally has an E-W strike direction with a northerly dip.

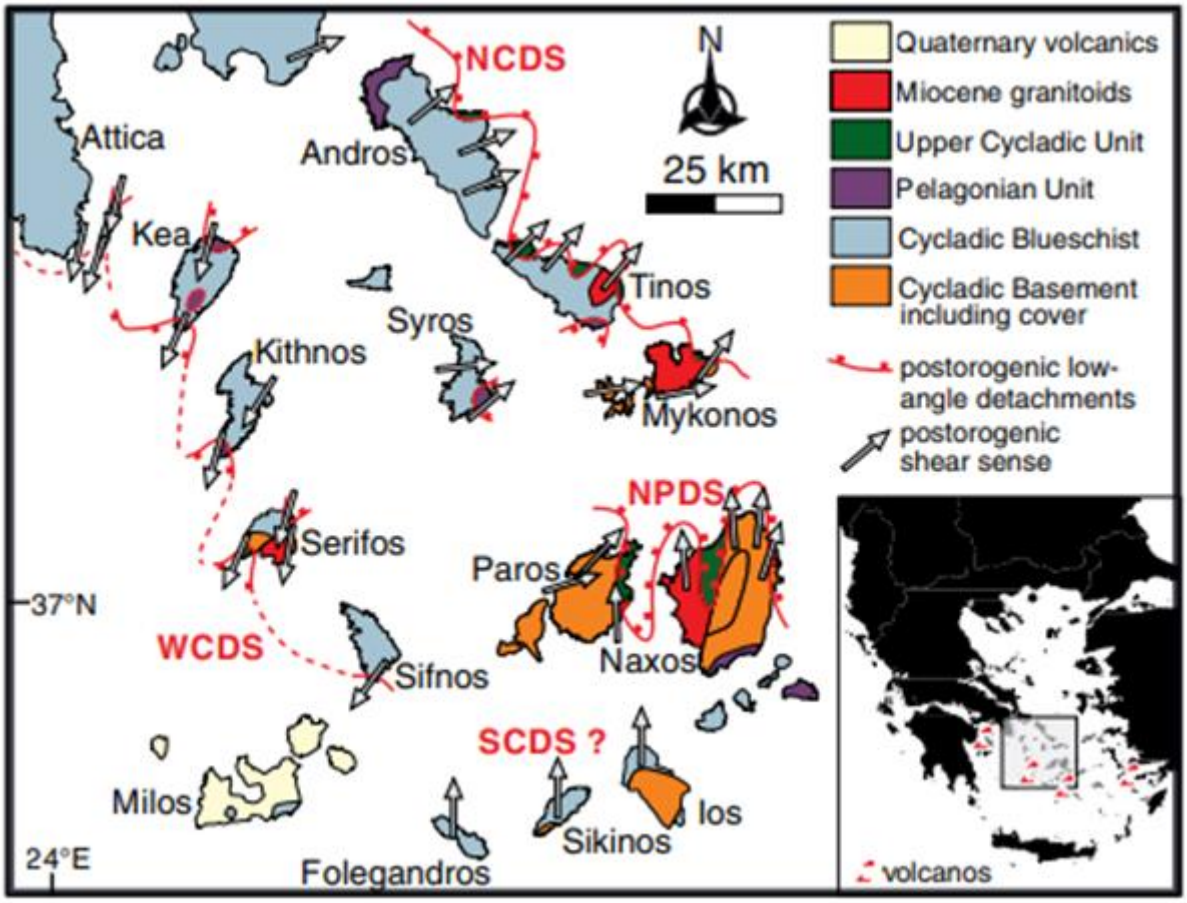

Figure 5. Geological Map of the Cycladic detachment system. WCSD—West Cycladic detachment system from Sifnos to Lavrion, Attica. NCSD—North Cycladic detachment system, NPDS—Naxos-Paros detachments system, and SCDS—South Cycladic detachment system. Inset shows the major active volcanoes (Grasemann et al., 2018).

2.3 Types of mineralization

The Lavrion mining district is a worldwide unique deposit including five types of mineralization, here listed in order of highest metal content.

2.3.a Porphyry type (Mo-W)

An intrusion with high Mo-W mineralization is exposed in 300 × 400 m^2 area, west of Plaka (Voudouris et al., 2008; Bonsall et al., 2011). The quartz veins compound mainly of granular quartz, sericite and hydrothermal biotite and reach a thickness up to 40 cm with NW-SE strike direction. The Plaka granodiorite is altered by hydrothermal fluids into five alteration types (potassic, soda-potassic, prophylitic, sericitic and siliceous). The mineralization mainly consists of sulfides (pyrite, molybdenite, chalcopyrite and pyrrhotite), phosphates (monazite-(Ce) and xenotime-(Y)), silicates (zircon and thorite) and oxides (rutile and ilmenite). The sericite is composed primarily of secondary quartz; albite and orthoclase are less prominent (Voudouris et al., 2008; Kolitsch et al., 2015). The Serpieri deposit near Kamariza consists of microgranite dikes crosscut by stockworks interbedded with a mixture of pyrrhotite, arsenopyrite, pyrite and galena. The carbonate-sericite alteration of the host rock is overlain by secondary biotite and K-feldspar during an early potassic alteration event (Voudouris et al., 2018).

2.3.b Skarn type (Fe-Cu-Bi-Au-Te)

The skarn type deposit is situated near the Plaka granodiorite intrusion hosted in Kamariza schist and lower and upper marbles (Leleu et al., 1973; Economou et al., 1981; Voudouris et al., 2008). The skarn deposit could not have been formed in the low thickness acid veins. The skarn type mineralization sequence consists of early magnetite, pyrrhotite, pyrite, arsenopyrite, sphalerite, chalcopyrite, and Bi-Ag-rich galena. The metal content in the skarn changes close to the Plaka granodiorite. Magnetite, magnetite-hematite is close to granodiorite in the upper marble. Pyrite-pyrrhotite, sphalerite-pyrite-galenite far distantly to granodiorite in Kamariza schist (Bonsall et al., 2011). A modest garnet-rich skarn deposit is found in Serpieri mine. The microgranite dikes are associated with the Lower marble. It contains prograde mineralization consisting of andradite, wollastonite, apatite and magnetite. Aggregates of retrograde stage are constituted by calcite, actinolite, epidote, chlorite, quartz, hematite, pyrite, chalcopyrite and pyrrhotite (Voudouris et al., 2018).

2.3.c Carbonate-replacement mineralization (Pb-Zn-Cu-Ag-Au, skarn-free)

This deposit type is the most important in the Lavrion mining district. The ore body is best distinguished in the Kamariza area, with an extension of several tens of meters. The Pb-Zn-Cu-Ag-Au mineralization occurs in the form of Mantos type, stratified lenses to displacement layers and Chimney type (across the stratification in marble) and consists of pyrite, sphalerite, chalcopyrite, and galena. The gangue minerals are quartz, fluorite, and calcite. The skarn-free orebody is underlain by pro and retrograde skarn, and overlain by vein-type phase. Marble is mainly located in the Kamariza unit and the Lavrion blueschist unit. The host rock consists of hydrothermal dolomite, calcite, siderite, ankerite, quartz and sericite (Marinos et al., 1956; Voudouris et al., 2003; Skarpelis, 2007; Voudouris et al., 2008; Scheffer et al., 2017; Scheffer et al., 2019; Voudouris et al., 2021).

2.3.d,e Pb-Zn-Ag-Au epithermal veins and breccias

Besides the carbonate replacement mineralization, the youngest of all deposits, the Pb-Zn-Ag-Au epithermal veins and breccias is the second important mineralization type in the Lavrion area. It occurs in several areas eg. Thorikos, Kamariza, Spitharopoussi, Ari and Megala Pefka and at the spots "Km 3", Esperanza, Sounio and Avlaki. The most valuable deposit is located about 800 m east of the Plaka granodiorite and is known as “Vein 80” or “Filoni 80” (Voudouris et al., 2008; Scheffer et al., 2017; Scheffer et al., 2019). This vein system is about 2 m wide and extends from ESE to WNW for about 1 km. Cleavage and veins cut through hornfels and are located in the Lavrion unit marble, Upper- and Lower marble and Kamariza schist. The veins formed upon penetration of the rock in brittle state by seawater and meteoric fluids (Bonsall et al., 2011; Berger et al., 2013; Scheffer et al., 2017; Scheffer et al., 2019). Vein 80 has a high silver content of up to 6000 ppm bound in Ag-sulfosalts (pyrargyrite, proustite, stephanite, ramdohrite, fizélyite, freieslebenite, marrite and Ag-rich members of the tetrahedrite group). A gold-rich deposit is located at Clemence in the Kamariza district, this native gold (>100 g/t) is associated with bismuthinite, gersdorffite, and galena (Voudouris, 2018).

2.4 Historical

The silver mines of Lavrion were the largest European mining area of antiquity. The mining industry started 4000 years ago until the last mine in Plaka closed in 1977. Through the decades, about 5500 km of tunnels were struck; approximately 2500 km are accessible (Conophagos, 1980). Marble tunnels were mainly built in the Soureza district (Legrena Valley) in antiquity. The solid tunnel construction makes it still possible to enter them safely today, unlike modern tunnels, which are located mostly in slate-formations. Due to the rapid advance in undermining for ore extraction, the walls must be supported. The wooden pillars were no longer maintained after the mines were closed. For this reason, many routes have collapsed (Rieck, 2012).

2.5 Type locality

The oxidation zone of the primary ores has a thickness of 250 m and is partially below the present groundwater table. The supergene oxidation of the ore forms the oxidation zone, and polymetallic sulfides, mainly pyrite, chalcopyrite, galena, and sphalerite, accompanied by the gangue minerals quartz, fluorite, and calcite (Kolitsch et al, 2015). The water entering the area has incised a valley depression. The oxidation process of hypogene sulfides began with the mixing of acidic water and marble, and reprecipitation occurred in open spaces.
At the Lavrion area, 639 primary and supergene minerals have been determined. The Lavrion mining district yielded type localities for more than 20 species (mereiterite, niedermayrite, attikaite, glaucocerinite, katsarosite, ktenasite, kapellasite, hilarionite, stergiouite, zincolivenite, agardite-(Nd), nickeltsumcorite, kamarizaite, and serpierite, and several Cd-Zn-bearing sulfates such as low mayrite, lazaridisite, voudourisite, drobecite, and katerinopoulosite from the Esperanza mine (Kokkoros, 1950; Giester & Rieck, 1995; Giester et al., 1998; Krause et al., 2006; Chukanov et al., 2007a, b; Chukanov et al., 2010; Giester &

Rieck, 2010; Pekov et al., 2011, 2013, 2016; Chukanov et al., 2018; Rieck et al., 2019; Rieck et al., 2020a, b).

2.6 Objectives

The Lavrion area in Attica, Greece, offers unique conditions for the formation various minerals in the ore deposits. In the Lavrion mining district, which extends over an area of 150 km^2 with over 5500 km of partially accessible tunnels, many areas are still undiscovered (Conophagos, 1980). This work contributes to further scientific insight into the mineralogy of this complex area. The minerals, chosen to be studied in my master thesis, were analysed with techniques according to modern scientific standards.

3. Methods

The samples, provided for the present study, mostly consisted of tiny specimen with individual crystals only visible under the microscope. The phases were stable and did not require further preparation. Several selected methods were applied to accurately determine the probe material, i.e. selected fragments were characterized with single-crystal X-ray diffraction, Raman spectroscopy, infrared spectroscopy and further by chemical analysis.

3.1 Single-crystal X-ray diffraction

The single-crystal X-ray diffraction data were collected at room temperature (bismoclite) or at 200K (guérinite) using a Bruker APEX II diffractometer equipped with a charge-coupled device (CCD) area detector and an Incoatec Microfocus Source IμS (30 W, multilayer mirror and MoKα). Tzeferisite data were obtained at room temperature with a Nonius Kappa CCD single-crystal X-ray diffractometer using a Mo sealed-tube source and a graphite monochromator. Reflection data integration and multiscan absorption correction were processed by the Bruker APEX 3 suite package (Bruker, 2020) respectively the Enraf-Nonius software bundle. The crystal structures were solved by the ShelX-program package (Sheldrick, 2018/3) and refined within the graphical interface ShelXle by Hübschle et al., (2011).

3.2 Raman spectroscopy

Raman spectra were collected at room temperature using the dispersive LabRAM HR Evolution spectrometer. The system has a focal length of 800 mm and is equipped with an Olympus BX series optical microscope and a Si-based, Peltier-cooled CCD detector. Raman spectra were excited with the 532 nm line of a frequency-doubled Nd:YAG laser (10 mW at the sample surface) or the 473 nm emission of a diode laser (17 mW). An Olympus 50× objective (numerical aperture (N.A.) 0.55) with a long free working distance of 10.7 mm was used to focuse the laser light onto the sample surface. The Raman scattered light was dispersed using a diffraction grating with 1800 grooves per millimetre. The system was calibrated using the Rayleigh line, resulting in a wavenumber accuracy of better than 0.5 cm^{-1}. Spectra were fitted after background correction assuming combined Lorentzian-Gaussian band shapes. Raman spectra do not show significant variations depending on random orientations of crystals with respect to the electric field vector of the polarised laser beam.

Selected phases were additionally examined at liquid-nitrogen temperature (l-N_2; –192 to –196 °C), using a Linkam cooling stage. These measurements were done to better resolve bands related to hydrous species (OH^- and H_2O).

3.3 Infrared spectroscopy

Infrared spectroscopy data were collected at room temperature using a Bruker Tensor 27 FTIR spectrometer with a Bruker Hyperion microscope. The spectrometer operates with a glo(w)bar infrared source and a KBr beam splitter. The spectral resolution is 4 cm^{-1}. The IR microscope used a Cassegrain mirror condenser and objective (15×/N.A.=0.4), a square

aperture of 25×45 μm^2 and a MCT detector. The instrument control and data handling were performed using the Bruker OPUS 5.5 software. The crystal was placed on a circular metal aperture of 100 µm. The sample and backround spectra were averaged from 256 scans and acquired in the range of 550 to 6000 cm^{-1}.

3.4 Chemical analysis

The chemical analysis were performed in cooperation with Branko Rieck using a JEOL Hyperprobe JXA8530F equipped with a field-emission electron gun. The electron probe micro-analyser (EPMA) runs in wavelength dispersive X-ray spectrometer (WDS) mode with following setting: spotsize 9, accelerating voltage 10 kV, beam current 20 nA and the diameter of the electron beam on the sample surface was 30 µm. Calibrant materials were used InAs (As–Lα, Sb_2S_3 (Sb–Lα), wollastonite (Ca–Kα), and MgO syn. (Mg-Kα) (X-ray lines analysed are quoted in brackets), H_2O was calculated from the structure.

4. Guérinite

Guérinite was first discovered on two museum samples[1] labelled with different locations Schneeberg, Saxony and Richelsdorf, Hessia (Nefedov, 1961). The mineral was named after the chemist Henri Guérin, Professor at Paris-Sud University, Orsay, France, who synthesized the chemical compound and identified the phase $5CaO•2As_2O_5•10H_2O$ (Nefedov, 1961). Guérinite forms acicular to wedge-shaped, colorless crystals as rosettes and spherulites, 0.2-0.3 mm in size. Their luster is sub-vitreous, silky to pearly and the Mohs hardness is 1½. Powder X-ray analyses give the strongest lines (d-spacing in Å) 1.87 (8), 3.48 (7), 3.88 (6) 3.26 (5), 2.69 (5) and 2.47 (5) (Nefedov, 1961). Chemical analysis of 90 mg sample (Table 1) gave As_2O_5 49.76, CaO 30.06, H_2O 19.18, insoluble 0.40, sum. 99.40 wt. % and agreed with the formula $Ca_5H_2(AsO_4)_4•9H_2O$ (Pierrot, 1964).

The crystal structure of a synthetic sample was solved in space group $P2_1/n$, with unit cell parameters a = 17.63 (1), b = 6.734 (3), c = 23.47 (2) Å, β = 90.6 (1)°, R = 0.13 (Catti & Ferraris, 1974). They characterized the material as very poor with twins $\{\bar{1}01\}$ and/or aggregates around [010]. The analysis was ambiguous and the authors mentioned several options of structure details with two models (1) $Ca_5(HAsO_4)_2(AsO_4)_2•9H_2O$, Z=5, assuming "empty" cavities that accommodate not fully occupied additional Ca^{2+} atoms and (2) $Ca_6H_3(AsO_4)_5•10H_2O$, Z=4.

Catti and Ferraris (1974) state: “According to (1) the numbers of Ca atoms (25) and of H_2O molecules (45) in the cell are odd; since in $P2_1/n$ positions with odd multiplicity are not possible, there are several possibilities: (i) the structure is disordered; (ii) the chemical formula is different from (1); (iii) the space group is apparently but not exactly true; (iv) the observed symmetry is the result of further twinning.”

Finally, the authors preferred model (1) because the water loss from TGA data were similar to the study of Pierrot (1964).

Table 1. Chemical analyses of guérinite [in wt. %].

Guérinite	$Ca_6(HAsO_4)_3(AsO_4)_2•10½H_2O$		$Ca_5H_2(AsO_4)_4•9H_2O$	
	Investigated sample		Pierrot, R. (1964)	
	Ideal	Mine No. 145	Ideal	Literature
As_2O_5	50.97	51.21	49.95	49.76
CaO	29.85	30.01	30.47	30.06
H_2O	19.18	18.72	19.58	19.18
MgO		0.06		
sum	100.00	100.00	100.00	99.40

[1] Museum not mentioned

Figure 6. Guérinite, associated with white, needle-like rauenthalite (lower left) and deformed pharmacolite (right) on calcite matrix that is partially covered by tiny marcasite crystals (mainly left of guérinite) field of view is 3.0 mm. © Branko Rieck

4.1 Results

The single-crystal X-ray diffraction analyses of guérinite from the Lavrion mining district, Attica (Figure 6) were performed in the monoclinic space group $P2_1/n$ with unit cell parameters a = 17.631 (2), b = 6.731 (1), c = 23.388 (3) Å, β = 90.69 (1)°, V = 2775.2 (6) Å^3, Z = 4. The final R-values obtained are R1 = 0.051 and wR2 [F_o^2][1] = 0.0972 for 9732 reflection with $F_o > 4\sigma(F_o)$, the ideal formula proposed is $Ca_6(HAsO_4)_3(AsO_4)_2 \cdot 10½H_2O$ (Table 2).

Table 2. Crystal data and details of the intensity measurement and structure refinement for guérinite.

Crystal Data	**Guérinite**
formula	$Ca_6(HAsO_4)_3(AsO_4)_2 \cdot 10½H_2O$
space group	$P2_1/n$
a (Å)	17.631 (2)
b (Å)	6.731 (1)
c (Å)	23.388 (3)
β (°)	90.69 (1)
V (Å^3)	2775.2 (6)
Z	4
ρ_{calc} (g cm^{-3})	2.70 (6)
μ(MoKα) (cm^{-1})	7.18
Data collection and Refinement	
$2\theta_{max}$ (°)	73.0
GoF	1.12
unique data	13452
data with $F_o > 4\sigma(F_o)$	9732
parameters, restraints	456 / 35
R1 [for $F_o > 4\sigma(F_o)$][1]	0.0513
wR2 [for all F_o^2][1]	0.0972
Δ $\rho_{min/max}$ (eÅ^{-3})	-1.34 / 1.55

[1] $R1 = \Sigma \, | \, | F_o | - | F_c | \, | \, / \Sigma \, | F_o |$; $wR2 = [\Sigma w(F_o^2 - F_c^2)^2 / \Sigma w(F_o^2)^2]^{½}$;
$w = 1 / [\sigma^2 (F_o^2) + (a \times P)^2 + b \times P]$; $P = \{[\max(0 \text{ or } F_o^2)] + 2F_c^2\} / 3$

Chemical analysis yielded As_2O_5 51.21, CaO 30.01, MgO 0.06, H_2O 18.72 (by difference), for total 100 wt. % (Table 1). The layered crystal structure of guérinite forms by edge and corner linkage of CaO_n and AsO_4 polyhedra in direction [10$\bar{1}$] (Figure 7).

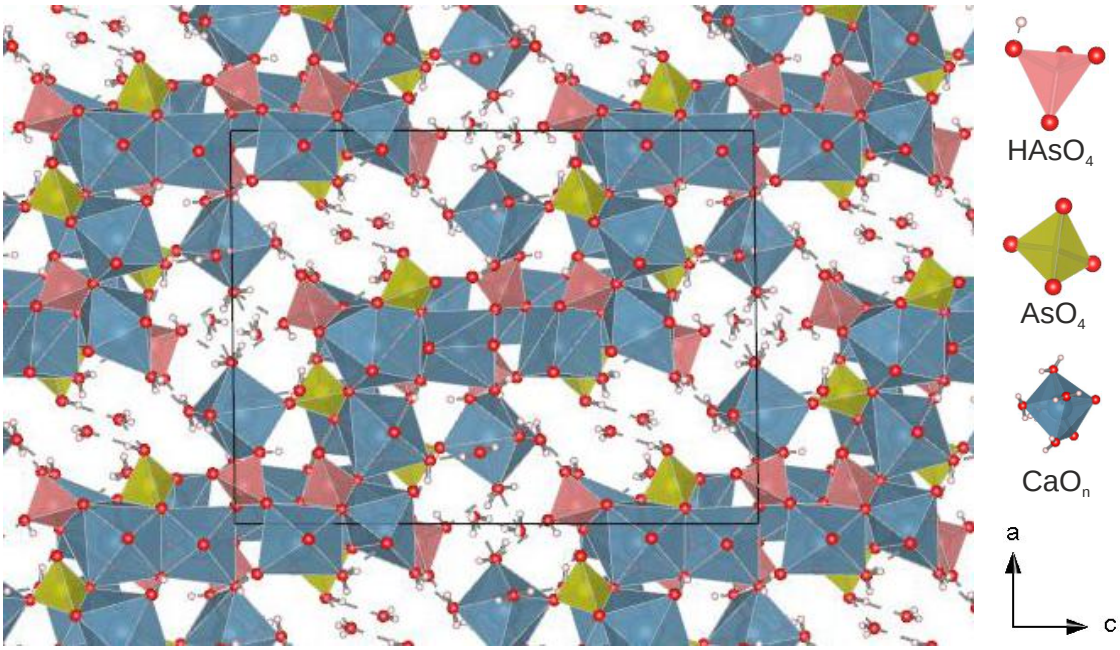

Figure 7. The layer structure of guérinite viewed along the **b** axis. All structure drawings were done with the VESTA software (Momma & Izumi, 2011).

Excluding hydrogen atoms, the asymmetric unit of guérinite contains five As^{5+} atoms, six Ca^{2+} atoms, and thirty O^{2-} atoms, all fully occupied. One free H_2O molecule (O_W10) is located between the layers. In addition a partially occupied site (50 % assumed based on the observed electron density of ~ 5e $Å^{-3}$) most probably belongs to a further H_2O molecule (O_W11), see Figure 8.

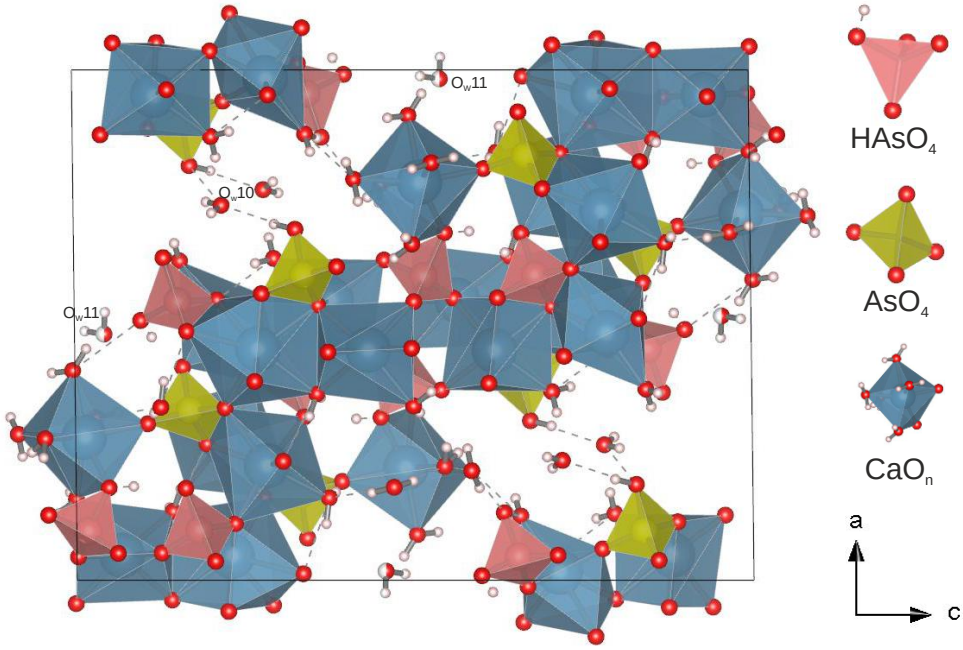

Figure 8. The free molecules O_W10 and O_W11 in the interlayer structure and the hydrogen bonding system (dotted lines) of guérinite.

Table 3. Atom coordinates and displacement parameters with estimated standard deviations [e.s.d.'s] in parentheses for guérinite.

ATOM	x	y	z	$U^{eq/iso}$	U^{11}	U^{22}	U^{33}	U^{23}	U^{13}	U^{12}
As1	0.59756 (2)	0.94821 (5)	0.33847 (2)	0.01254 (7)	0.01248 (16)	0.01096 (16)	0.01405 (15)	0.00002 (12)	– 0.00449 (12)	– 0.00028 (12)
As2	0.40165 (2)	0.25647 (5)	0.31869 (2)	0.00874 (6)	0.01043 (14)	0.00679 (14)	0.00892 (13)	0.00006 (11)	– 0.00319 (11)	0.00022 (12)
As3	0.33298 (2)	0.50994 (5)	0.16877 (2)	0.01005 (7)	0.01106 (15)	0.00903 (15)	0.00997 (14)	– 0.00115 (12)	– 0.00322 (11)	0.00045 (12)
As4	0.40417 (2)	0.37221 (5)	0.48311 (2)	0.00905 (7)	0.00979 (15)	0.00728 (14)	0.01003 (14)	0.00022 (11)	– 0.00262 (11)	– 0.00033 (12)
As5	0.54654 (2)	0.76768 (6)	0.15275 (2)	0.01711 (8)	0.01744 (18)	0.01635 (18)	0.01761 (17)	– 0.00074 (14)	0.00221 (13)	0.00294 (15)
Ca1	0.54951 (4)	0.42185 (10)	0.37966 (3)	0.01200 (12)	0.01394 (31)	0.01060 (29)	0.01137 (28)	0.00005 (23)	– 0.00382 (23)	0.00123 (24)
Ca2	0.45126 (4)	0.88460 (10)	0.43374 (3)	0.01138 (12)	0.01448 (31)	0.00874 (28)	0.01082 (27)	0.00040 (22)	– 0.00432 (22)	0.00126 (24)
Ca3	0.45301 (4)	0.77388 (10)	0.27077 (3)	0.01249 (12)	0.01345 (30)	0.00900 (29)	0.01490 (29)	– 0.00072 (23)	– 0.00449 (23)	0.00141 (24)
Ca4	0.51567 (4)	0.26605 (11)	0.21363 (3)	0.01631 (14)	0.02067 (35)	0.01324 (32)	0.01504 (30)	0.00168 (25)	0.00180 (26)	0.00569 (27)
Ca5	0.22420 (4)	0.50882 (10)	0.28183 (3)	0.01230 (12)	0.01337 (30)	0.00970 (28)	0.01370 (28)	– 0.00091 (23)	– 0.00554 (23)	0.00104 (24)
Ca6	0.21984 (5)	0.05904 (13)	0.48736 (3)	0.01857 (15)	0.01847 (35)	0.02432 (39)	0.01285 (30)	0.00320 (28)	– 0.00293 (25)	– 0.00539 (30)
O1	0.5613 (2)	1.0257 (4)	0.2768 (1)	0.0188 (5)	0.0222 (14)	0.0202 (14)	0.0140 (12)	0.0046 (10)	– 0.0044 (10)	0.0014 (11)
O2	0.6876 (2)	0.8531 (6)	0.3277 (2)	0.0325 (8)	0.0157 (15)	0.0400 (20)	0.0418 (20)	– 0.0089 (16)	– 0.0040 (13)	0.0102 (14)
O3	0.5389 (2)	0.7670 (4)	0.3600 (1)	0.0154 (5)	0.0157 (12)	0.0119 (12)	0.0186 (12)	0.0014 (10)	– 0.0028 (9)	– 0.0007 (10)
O4	0.6143 (2)	1.1185 (4)	0.3884 (1)	0.0226 (6)	0.0329 (16)	0.0153 (13)	0.0194 (13)	– 0.0048 (11)	– 0.0125 (12)	0.0020 (12)
O5	0.3895 (2)	0.0908 (4)	0.2654 (1)	0.0137 (5)	0.0167 (12)	0.0103 (11)	0.0140 (11)	– 0.0050 (9)	– 0.0072 (9)	0.0018 (9)
O6	0.4468 (2)	0.1541 (4)	0.3743 (1)	0.0142 (5)	0.0193 (13)	0.0127 (12)	0.0103 (11)	0.0021 (9)	– 0.0041 (9)	0.0007 (10)
O7	0.4631 (1)	0.4320 (4)	0.2954 (1)	0.0124 (5)	0.0132 (11)	0.0095 (11)	0.0144 (11)	0.0015 (9)	– 0.0025 (9)	– 0.0009 (9)
O8	0.3200 (1)	0.3640 (4)	0.3381 (1)	0.0150 (5)	0.0112 (11)	0.0181 (13)	0.0156 (12)	0.0006 (10)	– 0.0009 (9)	0.0028 (10)
O9	0.3064 (2)	0.6116 (4)	0.1067 (1)	0.0177 (5)	0.0230 (14)	0.0190 (13)	0.0108 (11)	– 0.0004 (10)	– 0.0058 (10)	0.0042 (11)
O10	0.3373 (2)	0.6836 (4)	0.2213 (1)	0.0142 (5)	0.0183 (13)	0.0118(11)	0.0125 (11)	– 0.0035 (9)	– 0.0063 (9)	0.0014 (10)
O11	0.4176 (2)	0.3996 (4)	0.1591 (1)	0.0175 (5)	0.0137 (12)	0.0189 (13)	0.0199 (13)	0.0004 (10)	– 0.0003 (10)	0.0052 (10)
O12	0.2672 (1)	0.3495 (4)	0.1938 (1)	0.0143 (5)	0.0114 (11)	0.0132 (12)	0.0181 (12)	– 0.0001 (9)	– 0.0012 (9)	– 0.0008 (9)
O13	0.4542 (2)	0.1685 (4)	0.4980 (1)	0.0141 (5)	0.0205 (13)	0.0069 (11)	0.0147 (11)	0.0002 (9)	– 0.0069 (10)	0.0034 (9)
O14	0.3189 (1)	0.2904 (4)	0.4515 (1)	0.0154 (5)	0.0113 (11)	0.0231 (14)	0.0116 (11)	0.0010 (10)	– 0.0028 (9)	– 0.0039 (10)
O15	0.3727 (2)	0.4899 (4)	0.5413 (1)	0.0156 (5)	0.0142 (12)	0.0195 (13)	0.0132 (11)	– 0.0063 (10)	– 0.0014 (9)	0.0020 (10)
O16	0.4475 (2)	0.5284 (4)	0.4390 (1)	0.0142 (5)	0.0176 (12)	0.0080 (11)	0.0172 (12)	0.0034 (9)	0.0007 (9)	– 0.0033 (9)
O17	0.4875 (2)	0.9555 (5)	0.1658 (1)	0.0278 (7)	0.0210 (15)	0.0249 (16)	0.0374 (18)	– 0.0130 (14)	– 0.0077 (13)	0.0109(12)
O18	0.5089 (2)	0.6223 (5)	0.0981 (1)	0.0285 (7)	0.0359 (18)	0.0315 (18)	0.0181 (14)	– 0.0061 (13)	0.0010 (13)	– 0.0001 (15)
O19	0.6319 (2)	0.8434 (5)	0.1321 (2)	0.0290 (7)	0.0221 (15)	0.0254 (17)	0.0397 (19)	– 0.0009 (14)	0.0122 (13)	– 0.0008 (13)
O20	0.5490 (2)	0.6205 (5)	0.2107 (1)	0.0221 (6)	0.0297 (16)	0.0184 (14)	0.0183 (13)	0.0032 (11)	– 0.0016 (11)	– 0.0053 (12)
H2	0.698 (4)	0.780 (8)	0.297 (2)	0.049						
H14	0.317 (3)	0.322 (8)	0.415 (1)	0.023						
H18	0.476 (5)	0.505 (14)	0.114 (4)	0.095 (30)						

O_w1	0.3652 (2)	0.7674 (4)	0.3573 (1)	0.0176 (5)	0.0177 (13)	0.0128 (12)	0.0221 (13)	0.0006 (10)	– 0.0089 (10)	– 0.0002 (10)
H1A	0.321 (2)	0.822 (7)	0.346 (2)	0.026						
H1B	0.358 (3)	0.638 (3)	0.363 (2)	0.026						
O_w2	0.3414 (2)	0.8699 (4)	0.4999 (1)	0.0198 (6)	0.0252 (15)	0.0131 (12)	0.0212 (13)	– 0.0001 (11)	– 0.0039 (11)	– 0.0007 (11)
H2A	0.328 (3)	0.748 (4)	0.510 (2)	0.030						
H2B	0.370 (3)	0.931 (7)	0.526 (2)	0.030						
O_w3	0.6306 (2)	0.4449 (7)	0.2956 (2)	0.0453 (11)	0.0446 (23)	0.0518 (26)	0.0401 (21)	0.0183 (19)	0.0203 (18)	0.0291 (20)
H3A	0.621 (4)	0.535 (8)	0.268 (2)	0.068						
H3B	0.671 (3)	0.372 (9)	0.289 (3)	0.068						
O_w4	0.6256 (3)	0.2463 (6)	0.1565 (2)	0.0579 (14)	0.0649 (30)	0.0278 (20)	0.0822 (34)	– 0.0022 (22)	0.0518 (26)	– 0.0021 (20)
H4A	0.660 (4)	0.339 (8)	0.149 (3)	0.087						
H4B	0.633 (4)	0.130 (6)	0.139 (3)	0.087						
O_w5	0.1611 (2)	0.4957 (5)	0.3736 (1)	0.0232 (6)	0.0258 (15)	0.0187 (14)	0.0251 (15)	0.0001 (12)	– 0.0024 (12)	0.0005 (12)
H5A	0.111 (12)	0.506 (8)	0.370 (2)	0.035						
H5B	0.173 (3)	0.371 (4)	0.383 (2)	0.035						
O_w6	0.2144 (2)	– 0.0561 (8)	0.5848 (2)	0.0510 (13)	0.0417 (23)	0.0858 (35)	0.0253 (18)	0.0237 (21)	– 0.0085 (16)	– 0.0301 (23)
H6A	0.181 (3)	– 0.149 (8)	0.596 (3)	0.077						
H6B	0.258 (2)	– 0.125 (10)	0.579 (3)	0.077						
O_w7	0.1820 (3)	– 0.2769 (6)	0.4698 (2)	0.0567 (13)	0.0953 (38)	0.0297 (21)	0.0444 (25)	0.0020 (18)	– 0.0275 (25)	– 0.0190 (23)
H7A	0.195 (5)	– 0.359 (9)	0.498 (2)	0.085						
H7B	0.171 (5)	– 0.336 (10)	0.437 (2)	0.085						
O_w8	0.0894 (3)	0.1131 (13)	0.5033 (3)	0.087 (2)	0.030 (3)	0.164 (7)	0.066 (4)	– 0.027 (4)	– 0.009 (2)	0.008 (3)
H8A	0.084 (5)	0.035 (14)	0.534 (3)	0.130						
H8B	0.047 (3)	0.131 (16)	0.483 (4)	0.130						
O_w9	0.2231 (3)	0.3742 (9)	0.5451 (2)	0.0646 (15)	0.058 (3)	0.079 (4)	0.057 (3)	– 0.026 (3)	0.025 (2)	– 0.038 (3)
H9A	0.250 (4)	0.275 (9)	0.565 (4)	0.097						
H9B	0.260 (4)	0.470 (9)	0.548 (4)	0.097						
O_w10	0.7348 (3)	0.7422 (9)	0.2189 (2)	0.0560 (12)	0.035 (2)	0.085 (4)	0.048 (3)	– 0.005 (3)	0.001 (2)	– 0.003 (3)
H10A	0.741 (5)	0.636 (7)	0.197 (3)	0.084						
H10B	0.719 (5)	0.857 (6)	0.204 (3)	0.084						
O_w11[2]	0.4823 (5)	0.1384 (18)	0.0436 (5)	0.061 (3)	0.036 (5)	0.075 (7)	0.072 (7)	0.034 (6)	0.005 (4)	– 0.007 (5)
H11A[2]	0.488 (10)	0.041 (24)	0.015 (5)	0.091						
H11B[2]	0.525 (6)	0.213 (21)	0.045 (7)	0.091						

[2] Half occupied

The description (atom labelling) of the refined model of guérinite was chosen analogue to Catti and Ferraris (1974) definitions except for the H_2O molecules which have been renamed to O_W1 – O_W11 (Table 3). The geometry of the H_2O molecules during refinement was stabilised by soft restraining. The proposed hydrogen bonding system in guérinite is indicated by medium to weak hydrogen bonds with O–H···O distances between 2.63 and 3.16 Å. The donator hydrogen bond distances within the H_2O molecules listed in Table 4 were refined by soft restriction to 0.88 – 0.92 Å, with H–O–H angles ranging from 97 to 121°. The distance between the H–atoms and their oxygens of the protonated arsenate polyhedra is O2–H2 0.89, O14–H14 0.88 and O18–H18 1.05 Å. The average bond As–O distances (Table 5) were determined for the AsO_4 groups as follows As2 1.682 and As3 1.686 Å and for $HAsO_4$ polyhedra As1 1.684, As4 1.690 and As5 1.688 Å. CaO_n polyhedra average bond distances (Table 5) are 2.408 – 2.444 (CaO7) and 2.517 Å (CaO_8), interatomic angles are listed in Table 20 (appendix). The atomic arrangement (Figures 9 and 10) is characterized by $Ca^{2+}O_n$ polyhedra (n = 7, 8) and AsO_4 tetrahedra sharing corners (Ca1–Ca4, As1 and As4; Ca2–As1 and As4; Ca3–Ca5, As2 and As3; Ca4–Ca1, Ca5, As1, As3, and As5; Ca5–As2 and As3; Ca6–As3 and As4) and edges (Ca1–Ca2, Ca3, As1 and As2; Ca2–Ca3; Ca3–Ca5, As1 and As5; Ca4–Ca3, As2; Ca5–As3).

Table 4. Hydrogen bonding scheme [Å, °] for guérinite.

D–H	d(D–H)	D–H···A	d(D–A)	∠(D–H···A)	(H–D–H)	∠(H–D–H)
O_W1–H1A	0.90 (2)	O_W1–H1A···O12	2.667 (4)	159 (5)	H1A–O_W1–H1B	108 (4)
O_W1–H1B	0.89 (2)	O_W1–H1B···O8	2.863 (4)	153 (5)		
O_W2–H2A	0.88 (2)	O_W2–H2A···O15	2.787 (4)	141 (5)	H2A–O_W2–H2B	114 (4)
O_W2–H2B	0.89 (2)	O_W2–H2B···O4	2.719			
O_W3–H3A	0.90 (2)	O_W3–H3A···O20	2.710 (5)	145 (7)	H3A–O_W3–H3B	113 (5)
O_W3–H3B	0.89 (2)	O_W3–H3B···O_W10	2.763 (6)	172 (7)		
O_W4–H4A	0.89 (2)	O_W4–H4A···O_W6	3.109 (7)	149 (7)	H4A–O_W4–H4B	114 (5)
O_W4–H4B	0.90 (2)	O_W4–H4B···O19	2.773 (5)	155 (7)		
O_W5–H5A	0.90 (2)	O_W5–H5A···O17	2.781 (4)	157 (5)	H5A–O_W5–H5B	109 (4)
O_W5–H5B	0.90 (2)	O_W5–H5B··O9	2.686			
O_W6–H6A	0.90 (2)	O_W6–H6A···O19	2.668 (5)	165 (7)	H6A–O_W6–H6B	104 (5)
O_W6–H6B	0.91 (2)	O_W6–H6B···O4	3.106			
O_W7–H7A	0.89 (2)	O_W7–H7A···O_W9	3.018 (8)	162 (7)	H7A–O_W7–H7B	115 (5)
O_W7–H7B	0.89 (2)	O_W7–H7B···O_W5	2.742 (5)	168 (7)		
O_W8–H8A	0.89 (2)	O_W8–H8A···O18	3.084		H8A–O_W8–H8B	125 (6)
O_W8–H8B	0.89 (2)	O_W8–H8B···O18	2.919 (6)	148 (9)		
O_W9–H9A	0.93 (2)				H9A–O_W9–H9B	97 (4)
O_W9–H9B	0.92 (2)	O_W9–H9B···O15	2.752 (5)	139 (7)		
O_W10–H10A	0.90 (2)	O_W10–H10A···O2	3.155 (7)	149 (7)	H10A–O_W10–H10B	121 (4)
O_W10–H10B	0.89 (2)	O_W10–H10B···O19	2.791			
O_W11–H11A	0.94 (4)	O_W11–H11A···O_W11	2.840 (2)	169 (15)	H11A–O_W11–H11B	109 (6)
O_W11–H11B	0.90 (9)	O_W11–H11B···O_W8	2.700 (11)	145 (15)		
O2–H2	0.89 (2)	O2–H2···O_W10	2.788 (6)	154 (6)		
O14–H14	0.88 (2)	O14–H14···O8	2.698 (4)	173 (5)		
O18–H18	1.05 (9)	O18–H18···O11	2.633 (5)	155 (8)		

Table 5. Selected interatomic bond distances [Å] and angles [°] for guérinite.

As1-O1	1.654 (3)	As2-O5	1.684 (2)	As3-O9	1.667 (3)
As1-O2[3]	1.733 (3)	As2-O6	1.666 (2)	As3-O10	1.697 (3)
As1-O3	1.688 (3)	As2-O7	1.697 (3)	As3-O11	1.684 (3)
As1-O4	1.661 (3)	As2-O8	1.679 (3)	As3-O12	1.694 (3)
<As1[4]-O>	<1.684>	<As2[4]-O>	<1.682>	<As3[4]-O>	<1.686>
As4-O13	1.665 (3)	As5-O17	1.668 (3)		
As4-O14[3]	1.755 (3)	As5-O18[3]	1.737 (3)		
As4-O15	1.675 (3)	As5-O19	1.666 (3)		
As4-O16	1.663 (3)	As5-O20	1.679 (3)		
<As4[4]-O>	<1.690>	<As5[4]-O>	<1.688>		
				Ca3-O1	2.555 (3)
Ca1-O3	2.375 (3)	Ca2-O3	2.459 (3)	Ca3-O3	2.564 (3)
Ca1-O4	2.348 (3)	Ca2-O6	2.285 (3)	Ca3-O5	2.412 (3)
Ca1-O6	2.558 (3)	Ca2-O13	2.322 (3)	Ca3-O7	2.378 (3)
Ca1-O7	2.478 (3)	Ca2-O13	2.431 (3)	Ca3-O10	2.411 (3)
Ca1-O15	2.365 (3)	Ca2-O16	2.402 (3)	Ca3-O17	2.815 (4)
Ca1-O16	2.396 (3)	Ca2-O_w1	2.462 (3)	Ca3-O20	2.441 (3)
Ca1-O_w3	2.449 (4)	Ca2-O_w2	2.496 (3)	Ca3-O_w1	2.562 (3)
<Ca1[7]-O>	<2.424>	<Ca2[7]-O>	<2.408>	<Ca3[8]-O>	<2.517>
Ca4-O1	2.328 (3)	Ca5-O5	2.343 (3)	Ca6-O9	2.270 (3)
Ca4-O5	2.806 (3)	Ca5-O8	2.342 (3)	Ca6-O14	2.494 (3)
Ca4-O7	2.409 (3)	Ca5-O10	2.444 (3)	Ca6-O_w2	2.507 (3)
Ca4-O11	2.317 (3)	Ca5-O10	2.727 (3)	Ca6-O_w6	2.410 (4)
Ca4-O17	2.419 (3)	Ca5-O12	2.367 (3)	Ca6-O_w7	2.391 (4)
Ca4-O20	2.458 (3)	Ca5-O12	2.450 (3)	Ca6-O_w8	2.363 (5)
Ca4-O_w4	2.371 (4)	Ca5-O_w5	2.431 (3)	Ca6-O_w9	2.514 (5)
<Ca4[7]-O>	<2.444>	<Ca5[7]-O>	<2.443>	<Ca6[7]-O>	<2.421>

[3] Protonated hydrogen atom

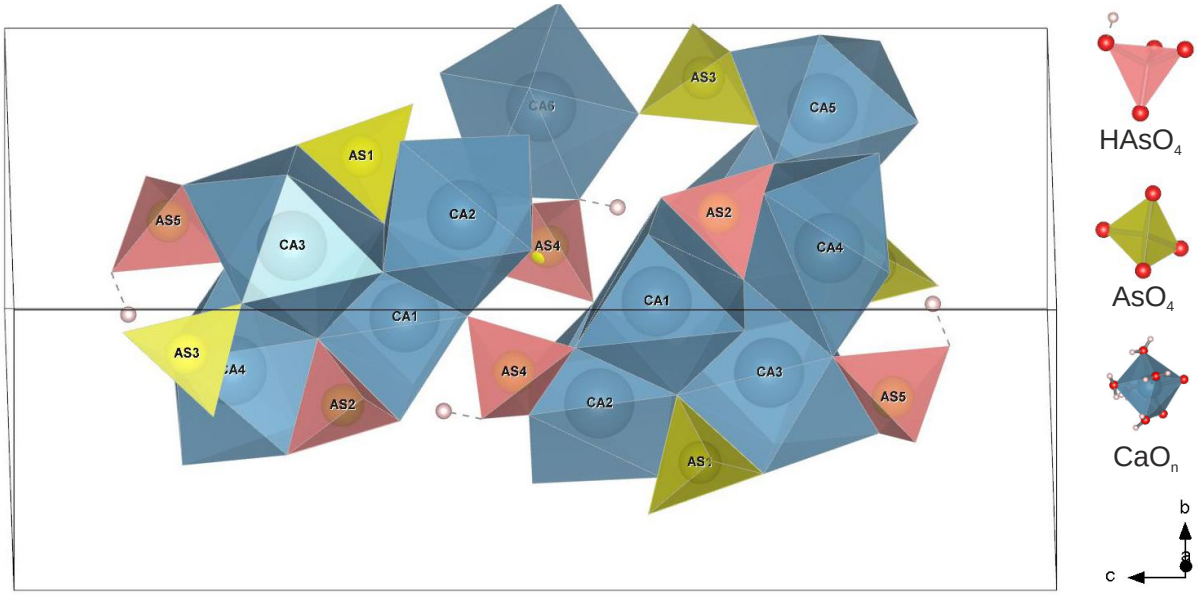

Figure 9. Linkage scheme of CaO_n polyhedra, AsO_4 and $HAsO_4$ tetrahedra of guérinite.

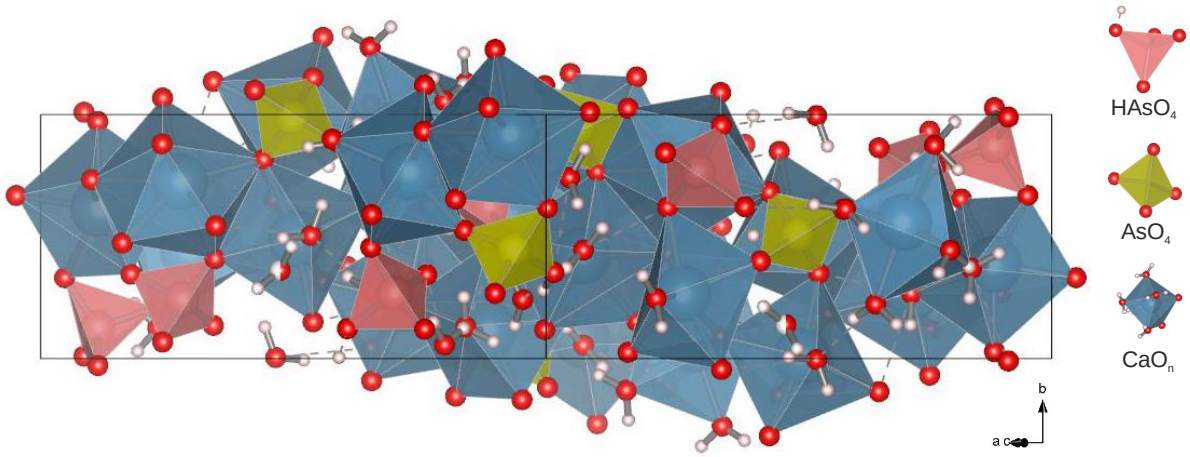

Figure 10. The layer structure of guérinite along [10$\bar{1}$].

The sum of bond strengths (calculated according to Brese & O'Keeffe, 1991, implemented within the Platon software (Spek, 2009) is shown in Table 6. CaO_n polyhedra provide average bond valences between 1.91 and 2.17 v.u. (valence units). The bond valence sums range between 4.95 and 5.04 v.u. for As^{5+} atoms. Protonated arsenate groups were identified by enlarged As–O distances values of 1.733, 1.755 and 1.737 Å for As1–O2, As4–O14 and As5–O18, respectively. Not considering contributions of the hydrogen atoms connected to the donor atoms (seen in Table 4) the calculation of bond valences leads to values of 1.10, 1.03 and 1.08 v.u. for O2, O14 and O18, respectively. The free O_W10 molecule is donor of hydrogen bonds to O2 (3.16 Å) and in addition is acceptor to O_W3 (2.76 Å). The H_2O molecules O_W1 – O_W9 are ligands exclusively to CaO_n polyhedra, resulting in following coordination: $Ca1O_6(O_W)_1$, $Ca2O_5(O_W)_2$, $Ca3O_7(O_W)_1$, $Ca4O_6(O_W)_1$, $Ca5O_6(O_W)_1$, and $Ca6O_2(O_W)_5$.

Table 6. Selected bond valence [v.u.] analysis for guérinite.

	As1[4]	As2[4]	As3[4]	As4[4]	As5[4]	Ca1[7]	Ca2[7]	Ca3[8]	Ca4[7]	Ca5[7]	Ca6[7]	sum
O1	1.36							0.20	0.38			1.94
O2	1.10											1.10
O3	1.24					0.33	0.26	0.20				2.03
O4	1.33					0.36						1.69
O5		1.25						0.30	0.10	0.36		2.01
O6		1.31				0.20	0.42					1.93
O7		1.21				0.25		0.33	0.30			2.09
O8		1.27								0.36		1.63
O9			1.31								0.44	1.75
O10			1.21					0.30		0.28+0.13		1.92
O11			1.25						0.39			1.64
O12			1.22							0.34+0.27		1.83
O13				1.32			0.29+0.38					1.99
O14				1.03							0.24	1.27
O15				1.28		0.34						1.62
O16				1.32		0.31	0.31					1.94
O17					1.31			0.10	0.29			1.71
O18					1.08							1.09
O19					1.31							1.32
O20					1.27			0.28	0.27			1.82
$O_{w}1$							0.26	0.20				0.46
$O_{w}2$							0.24				0.23	0.47
$O_{w}3$						0.27						0.27
$O_{w}4$									0.34			0.34
$O_{w}5$										0.29		0.29
$O_{w}6$											0.30	0.30
$O_{w}7$											0.32	0.32
$O_{w}8$											0.34	0.34
$O_{w}9$											0.23	0.23
sum	5.03	5.04	4.99	4.95	4.97	2.06	2.16	1.91	2.07	2.03	2.10	

4.2 Discussion

As already mentioned, Catti & Ferraris (1974) discussed two possible formulas for guérinite, (1) $Ca_5(HAsO_4)_2(AsO_4)_2$•9H2O with Z=5, and (2) $Ca_6H_3(AsO_4)_5$•$10H_2O$ with Z=4, preferring option (1) with the hypothesis (i) that some Ca in the crystal structure is partially disordered: the crystal structure contains “empty” cavities with measured residual electron densities (labelled St(1) and St(2)), which were seen as disordered calcium sites. In this case, the occupation factors are 0.17 (3) and 0.09 (3), respectively.
On the other hand, in the structure of guérinite six fully occupied Ca as well as five As positions are observed which are in accordance with model (2). The formula (1) $Ca_5(HAsO_4)_2(AsO_4)_2$•$9H_2O$ with unusual Z = 5 would further require two AsO_4 groups and two $HAsO_4$ groups distributed over five distinct As sites and is not fully explained.
The actual refinement (R1 = 0.051) results in average e.s.d.`s of interatomic distances which are more accurate by one order of magnitude (e.s.d.`s: As–O 0.003, Ca–O 0.003 and O–O 0.004Å) compared to the five decades old work (R = 0.13 with average e.s.d.`s Ca–O 0.04, O–O 0.05 Å). This allows a discussion of the present structure arrangement more in details. Between the layers a free, fully occupied H_2O molecule O_W10 occurs, similarly described as W10 by Catti and Ferraris. Contrary, the residual electrons densities St(1) and St(2) of Catti & Ferraris, (1974), assumed as disordered, partially occupied calcium atoms, more likely also represent disordered H_2O, the position St(1) fairly corresponds to the partially occupied H_2O molecule O_W11 in the present refinement, leading to the formula $Ca_6(HAsO_4)_3(AsO_4)_2$•$10.5H_2O$. Table 7 compiles the ideal chemical composition [in wt. %] calculated for different structure models of guérinite. It is evident that differences are very small, as already stated by Catti & Ferraris (1974).

Table 7. Ideal chemical composition [in wt. %] calculated for different structure proposals of guérinite compared with analytival data.

Guérinite Ideal	**$Ca_6(HAsO_4)_3(AsO_4)_2$•$10½H_2O$**	**$Ca_5H_2(AsO_4)_4$•$9H_2O$**	**$Ca_6H_3(AsO_4)_5$•$10H_2O$**
As_2O_5	50.97	49.95	51.38
CaO	29.85	30.47	30.09
H_2O	19.18	19.58	18.53
MgO			
sum	100.0	100.00	100.00

Measured data	**Present study Plaka mine No. 145**	**Pierrot, R. (1964) Natural sample**	**Synthetic sample**	**Catti and Ferraris (1974) (1) Synthetic sample**	**(2) Synthetic sample**
As_2O_5	51.21	49.76	50.22	51.80	50.31
CaO	30.01	30.06	30.31	30.64	30.29
H_2O	18.72	19.18	19.63	17.56	19.40
MgO	0.06				
sum	100.00	99.40	100.16	100.00	100.00

Table 8. Selected bond valence [v.u.] analysis for guérinite from Catti & Ferraris (1974).

	As1	As2	As3	As4	As5	Ca1[7]	Ca2[7]	Ca3[8]	Ca4[8]	Ca5[7]	Ca6[7]	sum
O1	1.37							0.25	0.31			1.93
O2	1.23											1.23
O3	1.05					0.40	0.23	0.23				1.91
O4	1.30					0.39						1.69
O5		1.37						0.29	0.10	0.34		2.10
O6		1.49				0.25	0.33					2.07
O7		1.34				0.27		0.34	0.23			2.18
O8		2.00								0.26		2.26
O9			1.23								0.48	1.71
O10			1.37					0.30		0.12+0.24		2.03
O11			1.70						0.33			2.03
O12			1.61							0.21+0.29		2.11
O13				1.20			0.29+0.39					1.88
O14				1.04							0.22	1.26
O15				1.05		0.31						1.36
O16				1.66		0.26	0.26					2.18
O17					1.30			0.09	0.26			1.65
O18					0.94							0.94
O19					1.30							1.30
O20					1.34			0.21	0.20			1.75
O_w1							0.21	0.22				0.43
O_w2							0.29				0.20	0.49
O_w3						0.26			0.05			0.31
O_w4									0.34			0.34
O_w5										0.21		0.42
O_w6											0.31	0.31
O_w7											0.34	0.34
O_w8											0.26	0.26
O_w9											0.19	0.19
sum	4.95	6.20	5.92	4.94	4.87	2.13	1.99	1.92	1.81	1.68	1.99	

The average bond distances (Table 21, appendix) are 1.682 – 1.690 Å for arsenate groups and 2.408 – 2.517 Å for CaO_n polyhedra, compared to the results of Catti & Ferraris (1974) with values AsO_4 1.61 – 1.69 Å and CaO_n 2.40 – 2.52 Å. Calculation of the bond valences shows some differences for both refinements (Table 8). For the data of Catti & Ferraris (1974) bond valence ΣCa–O are 1.68 – 2.13 v.u. (CaO_7 polyhedra) and 1.81 – 1.92 v.u. (CaO_8 polyhedra). Describing the Ca4 atom to be seven-coordinated, the bond valence is reduced by 0.05 v.u. In the present study, calculations of bond valences yield less variations, i.e. 2.03 – 2.16 v.u. for CaO_7 polyhedra and 1.91 v.u. for $Ca3O_8$.

The arsenate groups reveal bond valences for As^{5+} of the arsenate tetrahedra of 4.95 – 5.04 v.u., while those based on the data of Catti & Ferraris (1974) vary from 4.87 (As5) to 6.20 (As2) v.u. These authors did not attempt to determine the protonated arsenate groups based on the bond valence calculations for the oxygen ligands in detail. $HAsO_4$ groups were only

identified by the O–O distances of the proposed hydrogen bonding system. As5, attached to O18, As4 to two equally bonded oxygens (O14 and O15) and As1 to O2, (but only by 50%), were assumed to be part of hydrogen arsenate groups, with the resulting formula of $Ca_5(HAsO_4)_2(AsO_4)_2 \cdot 9H_20$. Bond valences, recalculated for these protonated arsenate groups of Catti & Ferraris (1974), give 1.23 (O2), 1.04 (O14) or 1.05 v.u. (O15) and 0.94 v.u. (O18). The refinement of guérinite from Lavrion yields bond valences for oxygen ligands for three proposed protonated arsenate groups between 1.03 and 1.27 v.u., i.e. As1–O2 (1.10 v.u.), As4–O14 (1.03 v.u.) and As5–O18 (1.09 v.u.), respectively. Further, the oxygen ligand O19 of the protonated $HAs(5)O_4$ group exhibits 1.31 v.u. only, but contributes to 3 hydrogen bonds as acceptor atom.

The general hydrogen bonding scheme was already outlined by Catti & Ferraris (1974) based on O···O contacts, excluding edges of coordination polyhedra. For most H_2O molecules and O–H groups, the proposed acceptor oxygen atoms well agree with the present study. Differences can be seen only for O_w9. However, already Catti & Ferraris (1974) state, “different donor–acceptor schemes are possible within the system O15, W7 and W9”.

O_w11, which corresponds to the St(1) site of of Catti & Ferraris, can well be refined as an oxygen atom with occupation ½. Nearest neighbours is O_w8 (2.700 Å) as well as symmetry-related O_w11^4 (2.840 Å).

[4] Symmetry equivalent

Table 9. Compilation of various minerals and synthetic compounds, chemically related to guérinite.

Mineral	Proposed Formula	Space group	<Ca[6]-O>	<Ca[7]-O>	<Ca[8]-O>	<As[4]-O>	As-O_h	Literature
Guérinite	$Ca_6(HAsO_4)_3(AsO_4)_2$•10½H_2O	*P*2_1/*c*		2.408-2.444	2.517	1.682-1.690	1.733-1.755	Liebhart et al., 2021
	$Ca_5(HAsO_4)_2(AsO_4)_2$•9H_2O	*P*2_1/*n*		2.40-2.51	2.52-2.58	1.61-1.69	1.69-1.79	Catti & Ferraris, 1974
Ferrarisite	$Ca_5(HAsO_4)_2(AsO_4)_2$•9H_2O	*P*$\bar{1}$	2.340	2.439-2.427		1.687-1.688	1.739	Catti et al., 1980
Sainfeldite	$Ca_5(HAsO_4)_2(AsO_4)_2$•4H_2O	*C*2/*c*	2.346-2.381			1.689-1.690	1.726	Ferraris & Abbona, 1972
Vladimirite	$Ca_5(HAsO_4)_2(AsO_4)_2$•5H_2O	*P*$\bar{1}$	2.35	2.42-2.45		1.68-1.70	1.73	Catti & Ivaldi, 1981
	$Ca_4(HAsO_4)(AsO_4)_2$•4H_2O	*P*2_1/*c*		2.421-2.458	2.523	1.688-1.690	1.742	Yang et al., 2011
Jeankempite	$Ca_5(HAsO_4)_2(AsO_4)_2$•7H_2O	*P*$\bar{1}$	2.391	2.421-2.464		1.693-1.705	1.719-1.786	Olds et al., 2020
Haidingerite	$Ca(HAsO_4)$•H_2O	*Pcnb*		2.44		1.684	1.729	Ferraris et al., 1971
Weilite	$Ca(HAsO_4)$	*P*$\bar{1}$		2.46	2.496	1.679-1.690	1.704-1.722	Ferraris & Chiari, 1970
Pharmacolite	$Ca(HAsO_4)$•2H_2O	*Ia*			2.515	1.686	1.729	Ferraris et al., 1971
Phaunouxite	$Ca_3(AsO_4)_2$•11H_2O	*P*$\bar{1}$		2.412-2.434	2.518	1.685		Catti & Ivaldi, 1983
Rauenthalite	$Ca_3(AsO_4)_2$•10H_2O	*P*$\bar{1}$		2.42-2.45	2.54	1.67-1.69		Catti & Ivaldi, 1983
Svenekite	$Ca(HAsO_4)_2$	*P*$\bar{1}$		2.464		1.684-1.686	1.721-1.735	Ondrus et al., 2013

Guérinite belongs to a group calcium arsenates represented by several mineral species and synthetic compounds as well. A compilation of these chemically related compounds is listed in Table 9, mostly studied by the research group of Catti & Ferraris intensively.
Ferrarisite $Ca_5(HAsO_4)_2(AsO_4)_2•9H_2O$ (Catti et al., 1980), is reported as a polymorph of guérinite. The crystal structure is built up by each two CaO_7 polyhedra and AsO_4 tetrahedra, connected by edges and vertices, to form layers parallel (001). One more Ca^{2+} atom, six-coordinated to H_2O ligands, is located between the layers. Larger and smaller channels, along [010] and [100], respectively, are observed, housing disordered H_2O molecules.
Sainfeldite $Ca_5(HAsO_4)_2(AsO_4)_2•(H_2O)_4$ (Ferraris & Abbona, 1972), described as a dehydrated guérinite, has a framework structure, composed by three distorted CaO_6 octahedra as well as $HAsO_4$ and AsO_4 groups sharing edges and corners. Infinite chains of hydrogen bonds run along the **z** axis.
Vladimirite, described as $Ca_5(HAsO_4)_2(AsO_4)_2•5H_2O$ (Catti & Ivaldi, 1981), was later revised (Yang et al., 2011) to the new formula $Ca_4(HAsO_4)(AsO_4)_2•4H_2O$. Its structure is described by undulating layers parallel to (010), which are formed by four irregular CaO_n polyhedra [$Ca1O_6(H_2O)$, $Ca2O_6(H_2O)$, $Ca3O_4(H_2O)_3$ and $Ca4O_5(H_2O)_3$] connected by edges and vertices. The layers are interconnected by AsO_4 and $HAsO_4$ tetrahedra, as well as by hydrogen bonds along the **b** axis.
Jeankempite $Ca_5(HAsO_4)_2(AsO_4)_2•7H_2O$ (Olds et al., 2020) shows a crystal structure composed by CaO_n polyhedra, AsO_4 and $HAsO_4$ tetrahedra which are connected by edges and vertices to a framework structure. Vladimirite and jeankempite were considered to be formed by a topotactic reaction during the dehydration of guérinite.
CaO_7 polyhedra and $HAsO_4$ tetrahedra build the framework of haidingerite $Ca(HAsO_4)•H_2O$ (Ferraris et al., 1971), by neutron diffraction an unusual large H–O–H angle of 113° for the H_2O molecule, which forms non-linear bonds to the protonated arsenate group, was observed.
Weilite $Ca(HAsO_4)$ (Ferraris & Chiari, 1969) has a framework of inlayered CaO_7 and CaO_8 polyhedra linked by edges along the **x** axis and bonded chains by vertices along the **y** and ***z*** axes. The $HAsO_4$ tetrahedra are located on the layer surface and connected to the CaO_n polyhedra.
Pharmacolite $Ca(HAsO_4)•2H_2O$ (Ferraris et al., 1968) has a crystal structure with layers parallel (010) built by CaO_8 polyhedra and $HAsO_4$ tetrahedra. These layers are connected by a system of the hydrogen bonds via two H_2O molecules and the OH^- groups.
Phaunouxite $Ca_3(AsO_4)_2•11H_2O$ and rauenthalite $Ca_3(AsO_4)_2•10H_2O$ (Catti & Ivaldi, 1983) both build similar layer structures by CaO_n polyhedra and AsO_4 tetrahedra, connected by edges and vertices and the layers are linked by the hydrogen bonding system.
Svenekite $Ca(HAsO_4)_2$ (Ondrus et al., 2013) has a sheet structure formed by CaO_8 polyhedra and $HAsO_4$ groups connected by corners, the layers are stacked parallel to (001) and linked by the hydrogen bonding system.

5. Bismoclite

Bismuth as essential component so far has been reported for 230 mineral species (http://mindat.org, 2023, February 16). The majority belong to sulphides and sulfosalts (142), further oxides (23), sulfates (16) and the group of phosphates, arsenates and vanadates (37). Halides (5) are rather rare, e.g. gananite BiF_3, zavaritskite BiOF and bismoclite BiOCl (Mountain, 1935; Dolomanova et al., 1962; Jambor et al., 1988).
Bismoclite was discovered on sample No. 4465 (McGregor Museum, Kimberley) from Jakkalswater, South Africa, and determined by chemical analysis: Bi_2O_3 89.41, Cl 13.67, less $O=Cl_2$ 3.08, sum 100 wt. % (Mountain, 1935). At the same time, Bannister (1935) named bismoclite after its chemical composition and characterized it with the powder X-ray diffraction analyses. The crystal structure was determined on a synthetic sample in space group *P*4/*nmm*, with unit cell data a = 3.887 (5), c = 7.354 (5) Å, R = 9.17% (Keramides, 1993). A specimen from a Bi-Cu-Au deposit, Argentina was analyzed by powder X-ray diffraction (pXRD), inductively coupled plasma mass spectrometry (ICP-MS) for lithogeochemical methods, using an instrumental neutron activation analysis (INAA) with gravimetric group 4 packages, including 4F–Cl and 4F–$H_2O^{+/-}$, scanning electron microscopy (SEM), differential thermal analysis and thermogravimetric analysis DTA-TGA, and infrared spectroscopy (Testa, 2016). Recently, bismoclite was reported from the Jean Baptiste mine, Lavrion, Greece (Rieck et al., 2018); this material allowed for the first time a modern single-crystal X-ray diffraction study on a natural sample.
The bismoclite group (Dana classification 10.02.01, Gaines et al., 1998) includes the isotypic minerals zavaritskite BiOF (Aurivillius et al., 1964; Yatimov et al., 2022), bismoclite BiOCl (Bannister 1935; Mountain, 1935; Keramides, 1993) and daubréeite BiO(OH,Cl) (Domeyko, 1876; Bannister, 1935). Bismoclite is further isostructural with the minerals matlockite PbFCl (Bannister, 1934, Pasero & Perchiazzi, 1996), rorisite CaFCl (Liebich & Nicollin, 1977; Kulikov et al., 1982; Chesnokov et al., 1990), zhangpeishanite BaFCl (Sauvage, 1974; Shimazaki et al., 2008) and over 200 synthetic compounds with a triple combination following the matlockite–type system *M*F*X* (*M* = Ca, Sr, Ba, Sm, Eu, Pb; *X* = Cl, Br, I) (Weil & Kubel, 2001).

5.1 Results

A fragment of bismoclite was studied by single-crystal X-ray diffraction analysis in space group *P*4/*nmm* with unit cell parameters a = 3.887 (2), c = 7.357 (5) Å, Z = 2, V = 111.16 (14) $Å^3$ and refined to final values R1 = 0.0134 and wR2 = 0.0363 from 309 unique data with $F_o > 4\sigma(F_o)$. For the refinement of bismoclite, confirming the formula BiOCl, the description of atom positions and labelling was chosen analogue to Keramides (1993) using origin choice 2 at center 2/*m*. All atoms lie on special positions, the Wyckoff sites are at 2*c*: Bi, Cl and 2*b*: O with site symmetries of 4*mm* and 4*m*2, respectively.

Table 10. Crystal data and details of the intensity measurement and structure refinement for bismoclite.

Crystal Data	**Bismoclite**
formula	BiOCl
space group	*P4/nmm*
a (Å)	3.887 (2)
c (Å)	7.357 (5)
V (Å^3)	111.16 (14)
Z	2
ρ_{calc} (g cm^{-3})	7.781
μ(MoKα) (cm^{-1})	80.084
Data collection and Refinement	
2θmax (°)	90.66
GoF	1.206
unique data	319
data with $F_o > 4\sigma(F_o)$	309
Parameters/ restraints	10 / 0
R1 [for $F_o > 4\sigma(F_o)$]^1	0.0134
wR2 [for all F_o^2]^1	0.0363
$\Delta\ \rho_{min/max}$ (eÅ^{-3})	-2.56 / 2.94

^{1} $R1 = \Sigma\ ||F_o| - |F_c||\ /\ \Sigma\ |F_o|$; $wR2 = [\Sigma w(F_o^2 - F_c^2)^2\ /\ \Sigma w(F_o^2)^2]^{½}$;
$w = 1\ /\ [\sigma^2 (F_o^2) + (a \times P)^2 + b \times P]$; $P = \{[\text{max of } (0 \text{ or } F_o^2)] + 2F_c^2\}\ /\ 3$

The crystal data of bismoclite are listed in Table 10, the atom coordinates and displacement parameters in Table 11. The structure is composed of Bi^{3+} cations with each four O^{2-} and Cl^- ligands forming a tetragonal antiprism, which are connected as chains by sharing faces and edges along the $\mathbf{a}_1$ and $\mathbf{a}_2$ axes (Figures 11a and 11b) and show a layered structure within (001) (Figures 11c and 11d).

Table 11. Atom coordinates and displacement parameters with e.s.d.'s in parentheses for bismoclite. All atoms are on special Wyckoff positions, therefore U^{12}, U^{13} and U^{23} are zero.

ATOM	**x**	**y**	**z**	**$U^{eq/iso}$**	**$U^{11} = U^{22}$**	**U^{33}**
Bi	0.25	0.25	0.17044 (2)	0.00824 (6)	0.00801 (7)	0.00868 (8)
Cl	0.25	0.25	0.65 (2)	0.0125 (2)	0.0132 (3)	0.0111 (4)
O	0.25	0.75	0.5	0.0079 (5)	0.0072 (7)	0.0093 (11)

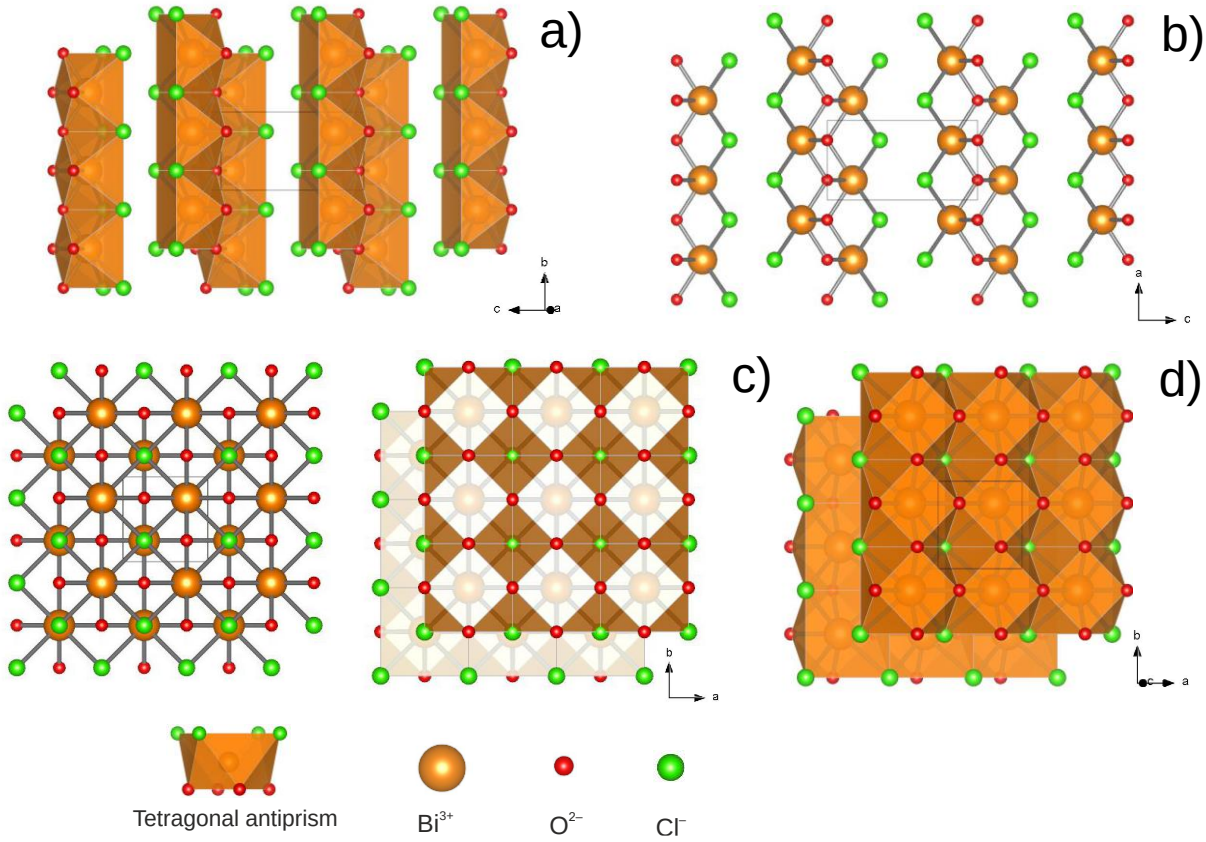

Figure 11. The layer structure of bismoclite. a) tetragonal antiprisms BiO_4Cl_4 form layers parallel (001), b) ball-and-stick model projected along [010], c) layer structure parallel to (001) (ball-and-stick model compared to representation by polyhedra), and d) respective layers viewed in a projection inclined by 15° illustrating linkage of polyhedra by edges and faces in directions [100] and [010].

Observed bond distances and angles of bismoclite as well as the bond valence sum for $Bi^{[8]}$ (parameters from Brese & O'Keeffe, 1991) are given in Table 12.

Table 12. Selected interatomic bond distances [Å], angles [°] and valences [v.u.] for bismoclite.

bond distances and angles			**bond valences**	
Bi–O	4×	2.3129 (1)	4×0.553	2.212
Bi–Cl	4×	3.0495 (6)	4×0.214	0.856
O–Bi–O	4×	72.91 (0)	$Bi^{[8]}$	<3.068>
O–Bi–Cl	8×	72.50 (2)		
Cl–Bi–Cl	4×	79.18 (2)		

A representative Raman spectrum of bismoclite yields the most intense Raman bands at 144 cm^{-1}, and minor bands are observed at 198 and 396 cm^{-1} (Figure 12).

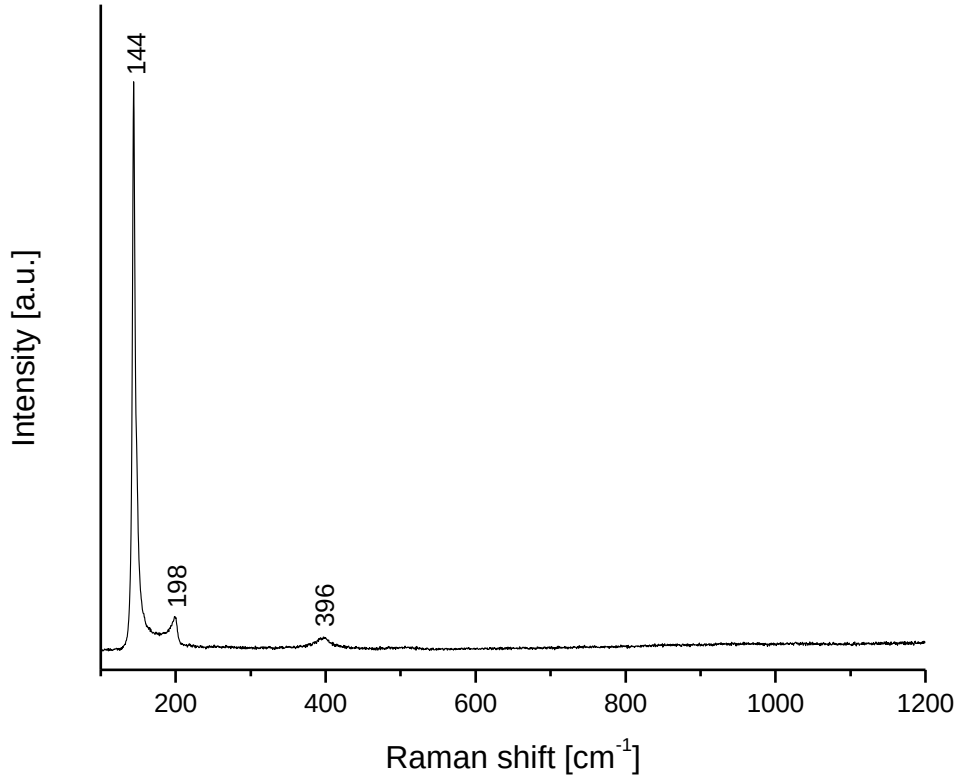

Figure 12. Raman spectrum (473 nm excitation) of bismoclite.

5.2 Discussion

The observed bands in the Raman spectrum at 144 and 198 cm^{-1} correlate with results of Bunda & Bunda (2013). The 396 cm^{-1} band observed herein was not detected by Bunda & Bunda (2013).

The Bi(III) cation has a $6s^2$ electron pair in the electron shell structure in the orbital model, which causes a lone pairs effect. These electrons are not involved in chemical bonding. Cations with $_ns^2$ electron pair (Tl(I), Pb(II), Sn (II), As(III), Bi(III), Sb(III), Se(IV), Te(IV), Br(V), I(V), respectively, are commonly asymmetrically coordinated with stereochemical activities of electrons. (Orgel, 1959; Galy et al., 1975).

The tetragonal antiprism of bismoclite has a Bi atom in the centre with four oxygen ligands on one side and four chlorine ligands on the other side. The four oxygen ligands form one face of the prism 1.2539 (2) Å away from the Bi atom, and the opposite face is formed by the chlorine ligands 1.3211 (14) Å away. The lone pairs are located near the surface of the chlorine atoms. This effect is also observable in the related minerals of bismoclite (see Table 13).

Table 13. Compilation of minerals and synthetic compounds, isostructural to bismoclite. Atoms are ordered in the following *AXY* system with *A* = Bi^{3+}, Pb^{2+}, Ca^{2+}, Ba^{2+}; *X* = O^{2-}, F^{-}; *Y* = Cl^{-}, F^{-}, OH^{-}.

Bond-	**Bismoclite BiOCl** This study	**Zavaritskite BiOF**[5] Aurivillius et al, 1964	**Daubréeite BiO(OH,Cl)** Bannister, 1935	**Matlockite PbFCl** Pasero & Perchiazzi, 1996	**Rorisite CaFCl**[5] Liebich & Nicollin, 1977	**Zhangpeishanite BaFCl**[5] Sauvage, 1974
distance *A*–*X* (Å) 4×	2.313 (1)	2.273 (2)	2.32	2.539 (1)	2.362	2.649
distance *A*–*Y* (Å) 4×	3.050 (6)	2.748 (2)	3.028	3.089 (4)	2.963	3.2856
distance *A*–*Y*[6] (Å) 1×	3.5283 (15)	2.920	3.4854	3.217	3.049	3.1960
valance sum $A^{[8]}$–*XY* (v.u.)	3.072	2.980	2.788	1.893	1.784	1.95
valance sum $A^{[9]}$–*XYY*[6] (v.u.)	3.131	3.061	2.833	2.012	1.944	2.205
Atom	**Wykoff position**					
Bi^{3+}	¼ ¼ 0.17044 (2)	¼ ¼ 0.2068 (3)	¼ ¼ 0.175			
Pb^{2+}				¼ ¼ 0.2058 (2)		
Ca^{2+}					¼ ¼ 0.1962 (12)	
Ba^{2+}						¼ ¼ 0.205
O^{2-}	¼ ¾ 0	¼ ¾ 0	¼ ¾ 0			
F^{-}				¼ ¾ 0	¾ ¼ 0	¾ ¼ 0
Cl^{-}	¼ ¼ 0.65 (2)		¼ ¼ 0.646	¼ ¼ 0.6497 (16)	¼ ¼ 0.6432 (14)	¼ ¼ 0.672
F^{-}		¼ ¼ 0.676 (9)				
OH^{-}			¼ ¼ 0.646			

[5] Data refer to synthesized phase

[6] Next nearest neighbour capping the tetragonal antiprism

Zavaritskite BiOF forms a tetragonal antiprism BiO_4F_4 with each four O^{2-} and F^- ligands; one further F^- ion is 2.92 Å apart (Aurivillius et al., 1964).
In the structure of daubréeite BiO(OH,Cl) (Domeyko, 1876) the Cl^- ligands are partially replaced by OH^- (Bannister, 1935).

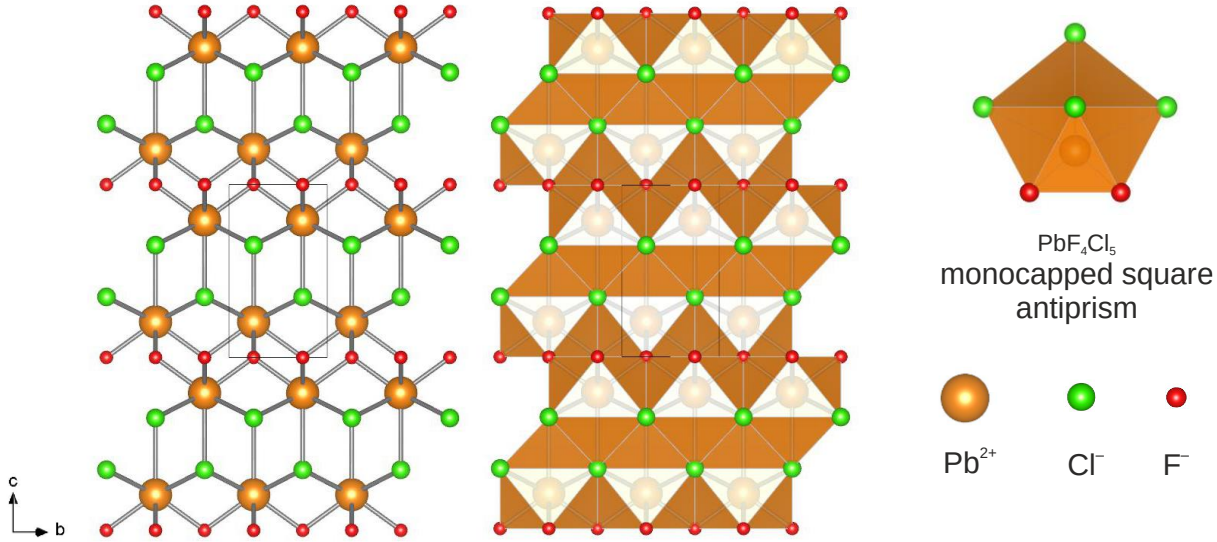

Figure 13. Structure of matlockite shown as ball-and-stick and polyhedra model.

The coordination polyhedra of the isostructural mineral matlockite PbFCl (Bannister, 1934) are commonly described as monocapped square antiprisms (Pasero & Perchiazzi, 1996), see Figure 13. This takes into account that the bond valence contribution of the ninth ligand is distinct. Even more pronounced as in matlockite, this is evident for the minerals rorisite CaFCl (Kulikov et al., 1982) and zhangpeishanite BaFCl (Shimazaki et al., 2008). Within the isotypic matlockite series the bond valence saturation of the cation significantly increases through the contribution of the ninth ligand, respective sums of bond valences for matlockite, rorisite and zhangpeishanite are listed in Table 13.
For the bismoclite group the description of bismuth with eight ligands, forming a tetragonal antiprism, seems appropriate. The bond valences sums for bismoclite, zavaritskite and daubréeite are 3.072, 2.980 and 2.788 v.u., respectively. Aurivillius et al. (1964), analyzing the coordination of each Bi cation, mentioned the additional 9th ligand. However, the bond valence contributions are only 0.059, 0.081, and 0.045 v.u. for bismoclite, zavaritskite and daubréeite, respectively, considered too weak to have a noticeable impact.

6. Tzeferisite

A phase with ideal formula $CaZn_8(SO_4)_2(OH)_{12}Cl_2•9H_2O$ was first discovered in slag dumps at Val Varenna, Italy. Based on single-crystal X-ray diffraction data the crystal structure was solved in space group $R\bar{3}c$, a = 8.3797 (4), c = 68.123 (5) Å, V = 4142.7 (9) $Å^3$, Z = 6, and refined to R = 4.9% (Burns et al., 1998).
Recently, colourless crystals grown on calcite matrix were isolated from a specimen found at the Ary Mine, Dimoliaki, Lavrion Mining District, Greece; by single-crystal X-ray diffraction identity with the slag phase described by Burns et al., 1998 was confirmed. In 2022 , the specimen was approved as a new mineral species (IMA No. 2022-094) (Rieck et al., 2023), named after Dr. Peter Tzeferis, a Greek Mining and Metallurgical Engineer.
Tzeferisite forms white, colorless, hexagonal, thin platelets and grows up to 60µm in size (Figure 14).

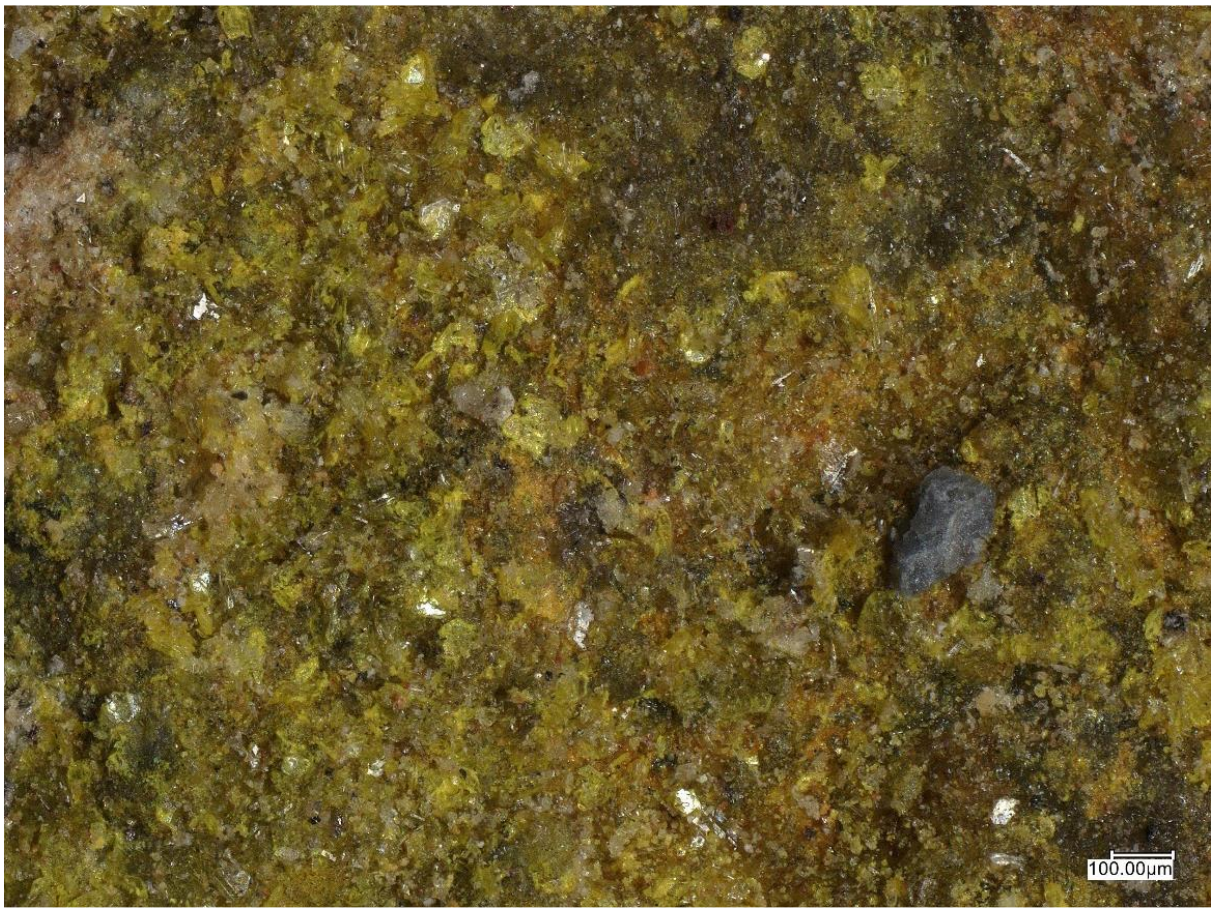

Figure 14. Tzeferisite, tiny colourless thin platelets, with associated mineral secondary greenockite on a calcite matrix. © Branko Rieck

Associated minerals are sphalerite, galenite, greenockite, hemimorphite, fabritzite, gypsum, calcite, dolomite. Chemical analysis by electron microprobe resulted in the empirical formula $Ca_{0.99}Zn_{8.02}(SO_4)_{1.99}(OH)_{12}Cl_{1.98}•9H_2O$, calculated on the basis of 30 H atoms per formula unit (apfu). The simplified formula is $CaZn_8(SO_4)_2(OH)_{12}Cl_2•9H_2O$ which requires SO_3 13.43, H_2O 22.66, $CaCl_2$ 9.31, ZnO 54.60, total 100 wt. %.
My contribution to the description of tzeferisite especially involved structure refinement and spectroscopic studies, therefore the chapter of the master thesis is restricted to this field.

Table 14. Crystal data and details of the intensity measurement and structure refinement for tzeferisite.

Crystal Data	**Tzeferisite**
formula	$CaZn_8(SO_4)_2(OH)_{12}Cl_2 \cdot 9H_2O$
space group	$R\bar{3}c$
a (Å)	8.3693 (12)
c (Å)	67.794 (14)
V (Å^3)	4112.5 (14)
Z	6
ρ_{calc} (g cm^{-3})	2.889
μ(MoKα) (mm^{-1})	7.52
Data collection and Refinement	
2θmax (°)	70.0
GoF	1.072
unique data	1989
data with $F_o > 4\sigma(F_o)$	1665
parameters, restraints	81 / 5
R1 [for $F_o > 4\sigma(F_o)$]^1	0.0356
wR2 [for all F_o^2]^1	0.089
$\Delta \rho_{min/max}$ (eÅ^{-3})	-0.99 / 1.66

^{1} $R1 = \Sigma \, | \, |F_o| - |F_c| \, | \, / \Sigma \, |F_o|$; $wR2 = [\Sigma w(F_o^2 - F_c^2)^2 / \Sigma w(F_o^2)^2]^{½}$;
$w = 1 / [\sigma^2 (F_o^2) + (a \times P)^2 + b \times P]$; $P = \{[\max of (0 \text{ or } F_o^2)] + 2F_c^2\} / 3$

6.1 Results

Crystal data for tzeferisite, space group $R\bar{3}c$, are listed in Table 14. Unit cell dimensions are a = 8.3693 (12), b = 8.3693 (12), c = 67.794 (14) Å, V = 4112.5 (14) Å^3,close to those reported for the slag phase by (Burns et al., 1998). The structure of tzeferisite could be refined to R1 = 0.0356, wR2 = 0.089. The labelling scheme was chosen in accordance to (Burns et al., 1998), the atom coordinates and displacement parameters are given in Table 15 and bond distances and angles in Table 16. The bond valence calculations are listed in Table 17 and the hydrogen bonding scheme in Table 18.

Table 15. Atom coordinates and displacement parameters with e.s.d.'s in parentheses for tzeferisite.

ATOM	x	y	z	$U^{eq/iso}$	U^{11}	U^{22}	U^{33}	U^{23}	U^{13}	U^{12}
Ca	0.66667	0.33333	0.08333	0.01756 (2)	0.01979 (4)	0.01979 (4)	0.01309 (5)	0	0	0.00990 (2)
Zn1	0.2860 (3)	0.41577 (4)	– 0.00074 (2)	0.01160 (1)	0.00675 (1)	0.00815 (1)	0.02006 (1)	0.00113 (1)	0.00036 (1)	0.00384 (1)
Zn2	0	0	– 0.02630 (2)	0.01169 (1)	0.00912 (1)	0.00912 (1)	0.01685 (2)	0	0	0.00456 (1)
S	0.33333	0.66667	0.04232 (2)	0.01238 (2)	0.01140 (3)	0.01140 (3)	0.01433 (4)	0	0	0.00570 (1)
Cl	0	0	– 0.05978 (2)	0.02221 (2)	0.02517 (3)	0.02517 (3)	0.01627 (4)	0	0	0.01259 (2)
O1	0.33333	0.66667	0.02032 (5)	0.01429 (5)	0.01484 (8)	0.01484 (8)	0.01319 (12)	0	0	0.00742 (4)
O2	0.3090 (4)	0.8190 (3)	0.04922 (3)	0.02913 (5)	0.05082 (14)	0.02977 (11)	0.02202 (9)	– 0.00882 (8)	– 0.00906 (9)	0.03155 (11)
OH3	0.4794 (2)	0.3743 (2)	0.01374 (3)	0.01111 (3)	0.00872 (7)	0.00834 (7)	0.01514 (7)	0.00050 (5)	0.00014 (5)	0.00343 (6)
OH4	– 0.1879 (2)	0.0597 (2)	– 0.01755 (3)	0.01154 (3)	0.00911 (7)	0.01002 (7)	0.01660 (7)	– 0.00022 (5)	– 0.00088 (5)	0.00561 (6)
O_W5	0.87789 (3)	0.55508 (3)	0.05780 (4)	0.02634 (4)	0.01970 (10)	0.02343 (10)	0.03223 (11)	0.00255 (8)	0.00486 (8)	0.00804 (9)
O_W6	0.66667	0.63627 (4)	0.08333	0.02497 (6)	0.02497 (15)	0.02463 (10)	0.02319 (13)	– 0.00059 (6)	0.00118 (11)	0.01417 (8)
H3	0.4766 (5)	0.362 (5)	0.02618 (4)	0.017						
H4	– 0.2287 (5)	0.0893 (5)	– 0.02842 (4)	0.017						
H6	0.5862 (5)	0.6674 (6)	0.07633 (6)	0.038						
H5A	0.9130 (6)	0.6764 (4)	0.06006 (6)	0.04						
H5B	0.9900 (4)	0.5641 (6)	0.05760 (7)	0.04						

Table 16. Selected interatomic bond distances [Å] and angles [°] for tzeferisite.

Ca–O_{w5}	6×	2.506 (2)	Zn1–O1		2.403 (2)
Ca–O_{w6}	3×	2.535 (3)	Zn1–OH3		2.039 (2)
<$Ca^{[9]}$–O_w>		<2.516>	Zn1–OH3		2.064 (2)
			Zn1–OH3		2.065 (2)
S–O1		1.491 (3)	Zn1–OH4		2.103 (2)
S–O2	3×	1.465 (2)	Zn1–OH4		2.108 (2)
<$S^{[4]}$–O>		<1.472>	<$Zn1^{[6]}$–O>		<2.131>
			Zn2–OH4	3×	1.965 (2)
			Zn2–Cl		2.270 (1)
O_{w5}–Ca–O_{w5}	3×	77.52 (9)	OH3–Zn1–OH3		81.55 (8)
	3×	77.58 (9)			96.26 (9)
	3×	87.45 (11)			174.74 (7)
	3×	134.38 (11)	OH3–Zn1–OH4		83.27 (7)
	3×	140.85 (11)			83.73 (7)
O_{w5}–Ca–O_{w6}	6×	67.19 (5)			97.30 (7)
	6×	70.42 (5)			100.98 (7)
	6×	136.28 (6)			101.87 (7)
OW6–Ca–Ow6	2×	120.00			166.83 (7)
			OH4–Zn1–OH4		91.88 (9)
O1–S–O2	3×	108.64 (10)	O1–Zn1–OH3		80.72 (6)
O2–S–O2	3×	110.31 (9)			81.23 (6)
					93.68 (6)
			O1–Zn1–OH4		86.28 (6)
					176.22 (8)
			OH4–Zn2–OH4	3×	111.26 (5)
			OH4–Zn2–Cl	3×	107.61 (6)

Table 17. Bond valence analysis for tzeferisite, calculated within the PLATON program suite (Spek, 2009) by parameters of Brese & O'Keeffe (1991).

	Ca	**Zn1**	**Zn2**	**S**	**sum**
Cl			0.50		0.50
O1		0.15 ×1↓ ×3 →		1.43	1.88
O2				1.62 ×3↓ ×1→	1.62
OH3		2× 0.38+0.40			1.16
OH4		2× 0.34	0.49 ×3↓ ×1→		1.17
O_{w5}	0.23 ×6↓ ×1→				0.23
O_{w6}	0.22 ×3↓ ×1→				0.22
sum	2.04	1.99	1.97	6.29	

Table18. Hydrogen bonding scheme [Å, °] for tzeferisite.

D–H	d(D–H)	D–H···A	d(D–A)	∠(D–H···A)
OH3–H3	0.85 (2)	OH3–H3···O_W5	3.011 (3)	175 (3)
OH4–H4	0.90 (2)	OH4–H4···S	3.512 (2)	142 (3)
OH4–H4	0.90 (2)	OH4–H4···O2	2.775 (3)	172 (3)
O_W5–H5A	0.92 (3)	O_W5–H5A···Cl	3.335 (2)	170 (4)
O_W5–H5B	0.90 (3)	O_W5–H5B···S	3.598 (2)	155 (4)
O_W5–H5B	0.90 (3)	O_W5–H5B···O2	3.204 (3)	134 (3)
O_W5–H5B	0.90 (3)	O_W5–H5B···O2	2.907 (4)	155 (4)
O_W6–H6	0.96 (2)	O_W6–H6···O2	2.807 (2)	142 (4)

The atomic arrangement of tzeferisite exhibits a complicated sheet structure. Two distinct Zn positions are present, Zn1 which is octahedrally coordinated by one O^{2-} and five OH^- ligands, and Zn2, tetrahedrally coordinated to three OH^- and one Cl^- atom (Figure 15).

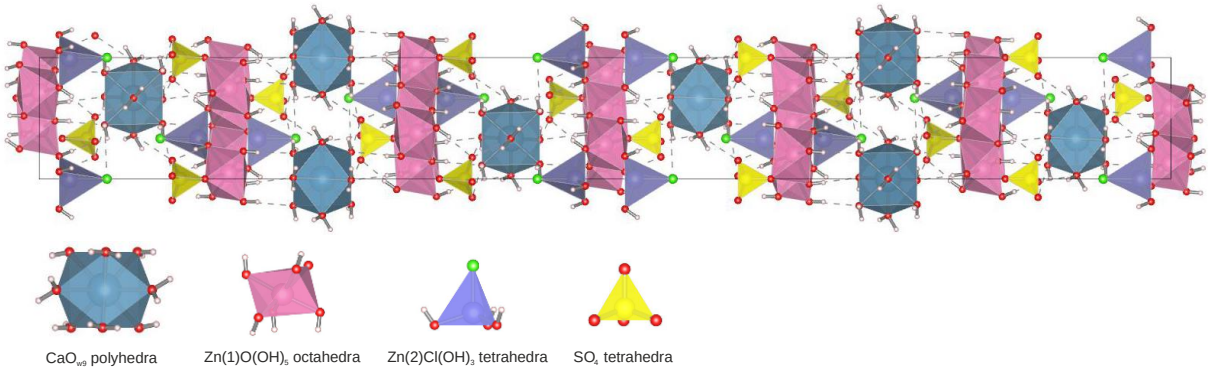

Figure 15. Crystal structure of tzeferisite projected parallel to [010].

The $Zn(1)O(OH)_5$ octahedra share edges to form brucite-like sheets with one-seventh of the octahedral sites vacant. The $Zn(2)Cl(OH)_3$ tetrahedra are attached to the sheet above and below the vacant site by sharing three OH^- anions with the $Zn(1)O(OH)_5$ octahedra. The single unique S^{6+} position is tetrahedrally coordinated by four O^{2-} anions and is linked to the tetrahedral-octahedral sheet by a single shared ligand. The unique Ca^{2+} cation is located in an interlayer position and is coordinated by nine H_2O molecules. H bonds provide strengthening within the tetrahedral-octahedral sheet, as well as the only linkages between the tetrahedral-octahedral sheets and the interlayer CaO_{w9} polyhedron.
The IR spectrum of tzeferisite is shown in Figure 16. The highest peaks are OH^- and H_2O stretching vibrations at 3319 and 3473 cm^{-1}, respectively. The H_2O bending mode is observed at 1643 cm^{-1} and the SO_4 stretching modes at 1124 and 999 cm^{-1}. The bands observed below 800 cm^{-1} are SO_4 bending modes and Me–O stretching and bending modes.

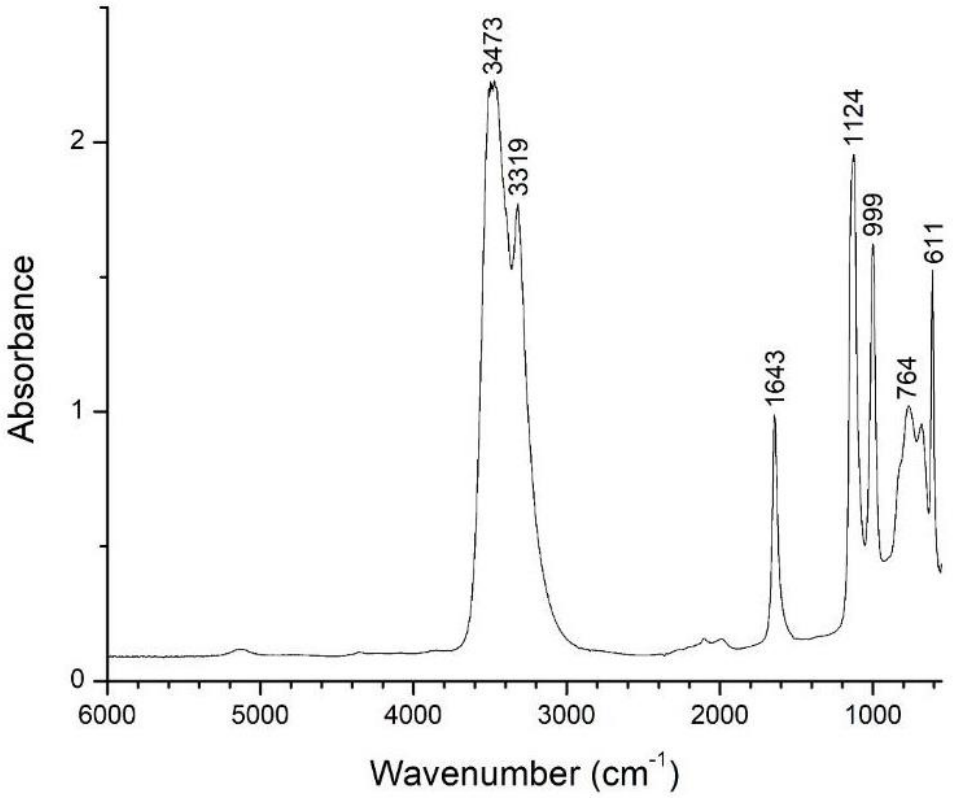

Figure 16. The infrared spectrum of tzeferisite.

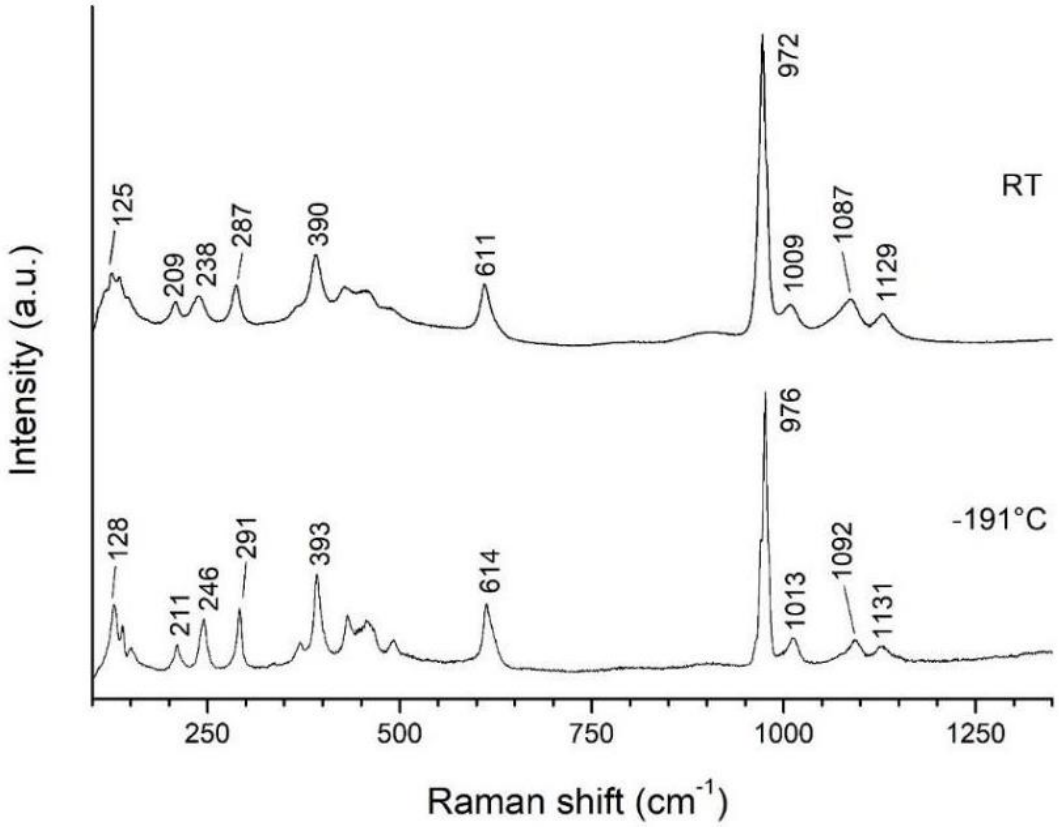

Figure 17. The Raman spectra show the intensity [a.u.] of the Raman shift [cm^{-1}] compared to the measurements at room temperature (RT, see above) and the N_2-cooled sample (–191°C) of tzeferisite.

The representative Raman spectra show strong intensities in the observed range 100 – 1350 cm^{-1} (Figure 17). Further, the most intense Raman bands are yielded at 972 cm^{-1}, and minor bands are observed from 125 to 614 cm^{-1} and from 1009 to 1131 cm^{-1}. The Raman bands provide a distinctive fingerprint for tzeferisite. The O–H stretching range is shown in Figure 18. At l-N_2 temperature, overlapping bands in the range 3300 – 3350 cm^{-1} are better resolved.

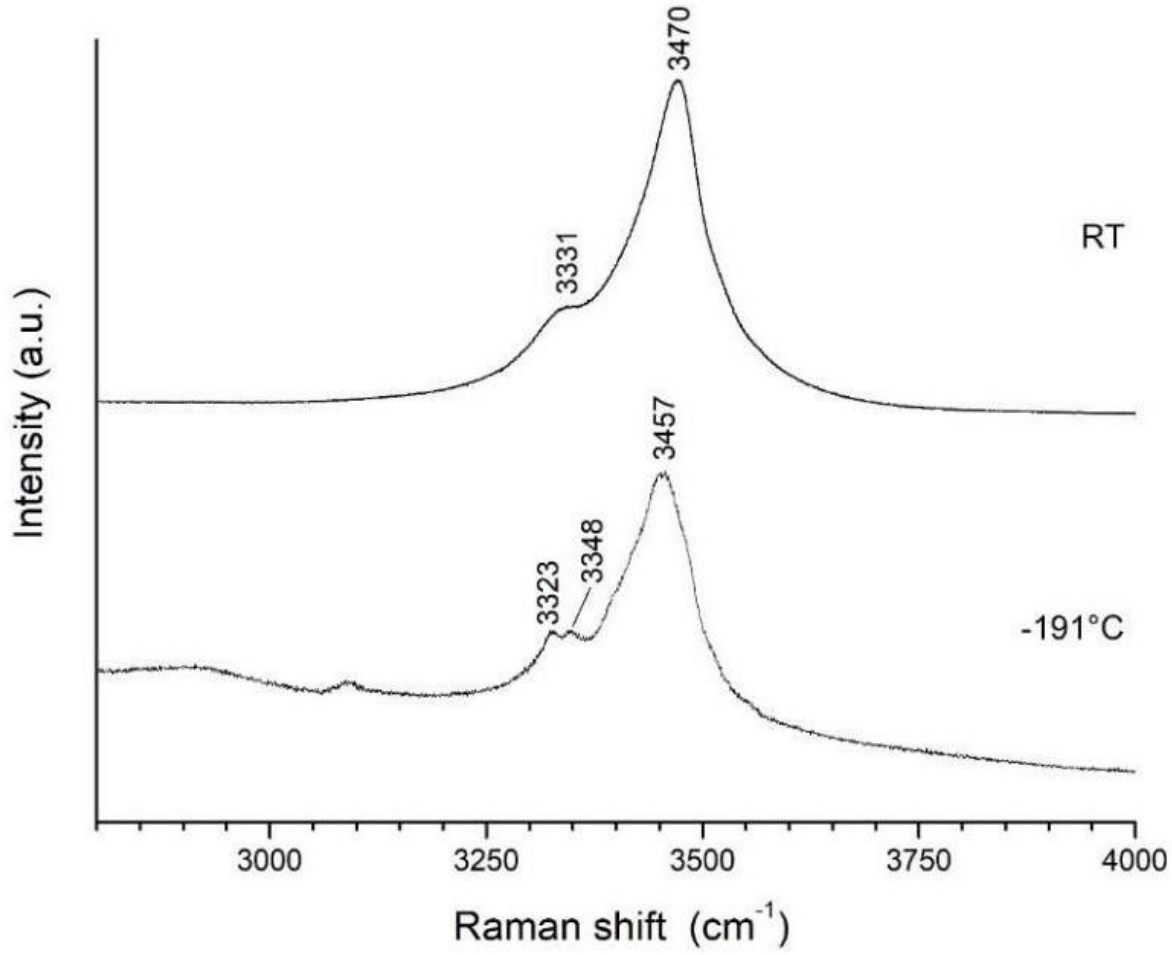

Figure 18. Raman spectra show the H_2O range comparing RT and N_2 cooling at –191°C based on the measurement of intensity [a.u.] and Raman shift [cm^{-1}] for tzeferisite

6.2 Discussion

Tzeferisite reveals brucite–type sheets of distorted $Zn(1)O(OH)_5$ octahedra (Figure 19) with bond distances of Zn1–O1 2.403, Zn1–OH3 2.040 – 2.066 and Zn1–OH4 2.104 – 2.108 Å and a bond valence sum 1.982 v.u. Attached to the layers, the $Zn(2)Cl(OH)_3$ tetrahedra (bond valence sum 1.698 v.u.) and the SO_4 tetrahedra (bond valence sum 6.047 v.u.) show bond distances of Zn2–OH4 1.965 and Zn2–Cl 2.270 and S–O 1.465 – 1.491 Å, respectively. The interlayered CaO_9 have Ca–O bond distances in the range 2.507 – 2.535 Å and yielded a bond valence strength of 2.041 v.u. for Ca^{2+}.

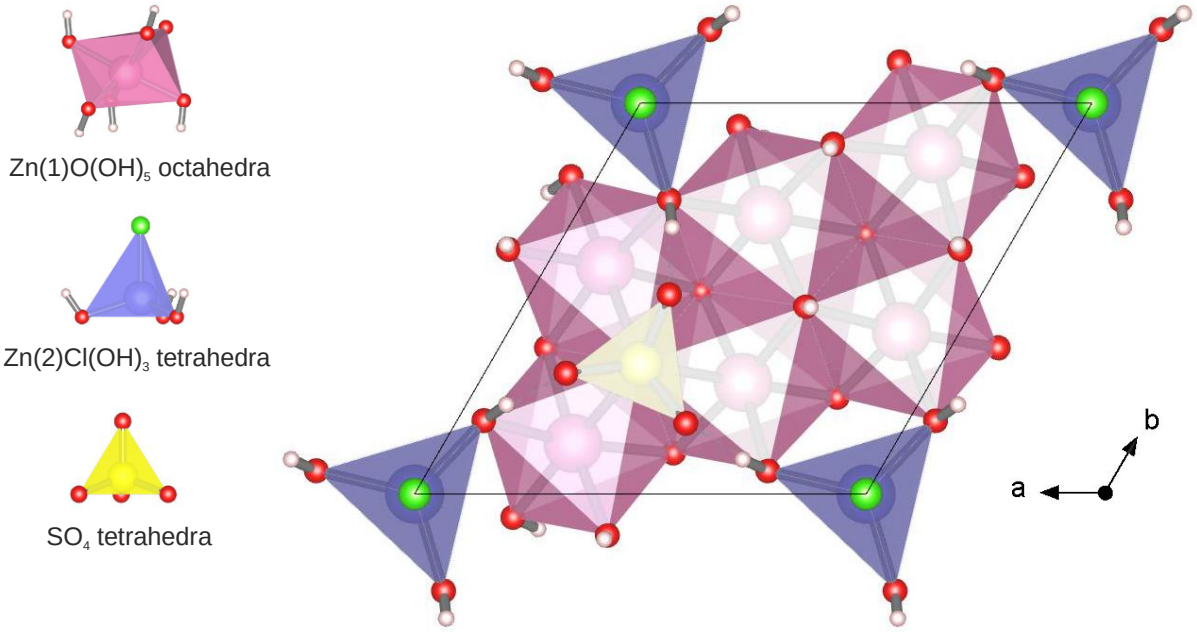

Figure 19. Brucite–type sheet of tzeferisite viewed along **c** axis.

The average values of the O–H bonds are OH–H 0.85 – 0.90 Å and O_W–H 0.90 – 0.96 Å. The distances between the donor and acceptor are within 2.775 – 3.598 Å and O–H···O angles between O_W5–O2 134° to OH3–O_W5 175°.

The mineral tzeferisite from the Lavrion mining district, Attica, Greece and the synthetic compound from the slag dumps at val Varenna, Italy exhibit the same crystal structure. Figure 20 shows the differences in the atomic arrangement of the involved polyhedra for the related phases of gordaite $NaZn_4(SO_4)(OH)_6Cl•6H_2O$ (Adiwidjaja et al., 1997; Zhu et al., 1997) and fabritzite $Zn_{0.5}Zn_4(SO_4)(OH)_6Cl•3H_2O$ (Kolitsch & Giester, 2013; Kolitsch et al., 2023), for easier comparison the formula was halved and reformulated, seen in Table 19. The brucite–type sheet of octahedra with attached $Zn(OH)_3Cl$ and SO_4 tetrahedra is present in all three compounds, only the interlayer cation and its arrangement is different between fabritzite, tzeferisite and gordaite (0.5 Zn^{2+}, 0.5 Ca^{2+}, and Na^{+}, respectively).

Table 19. Comparison of formula and crystal data of tzeferisite and related minerals and compounds.

Mineral	**Formula**	**Space group**	***a* (Å)**	***c* (Å)**	***V* (Å³)**	**References**
Tzeferisite	$Ca_{0.5}Zn_4(SO_4)(OH)_6Cl•4.5H_2O$	$R\bar{3}c$	8.3797 (4)	68.123 (5)	4142.7 (9)	Rieck et al., 2023
Fabritzite	$Zn_{0.5}Zn_4(SO_4)(OH)_6Cl•3H_2O$	$R\bar{3}$	8.275 (1)	32.000 (6)	1897.7 (5)	Kolitsch et al., 2023
Gordaite	$NaZn_4(SO_4)(OH)_6Cl•6H_2O$	$P\bar{3}$	8.3556 (3)	13.025 (1)	787.5	Adiwidjaja et al., 1997
Gordaite	$NaZn_4(SO_4)(OH)_6Cl•6H_2O$	$P\bar{3}$	8.413 (8)	13.095 (4)	803 (2)	Zhu et al., 1997

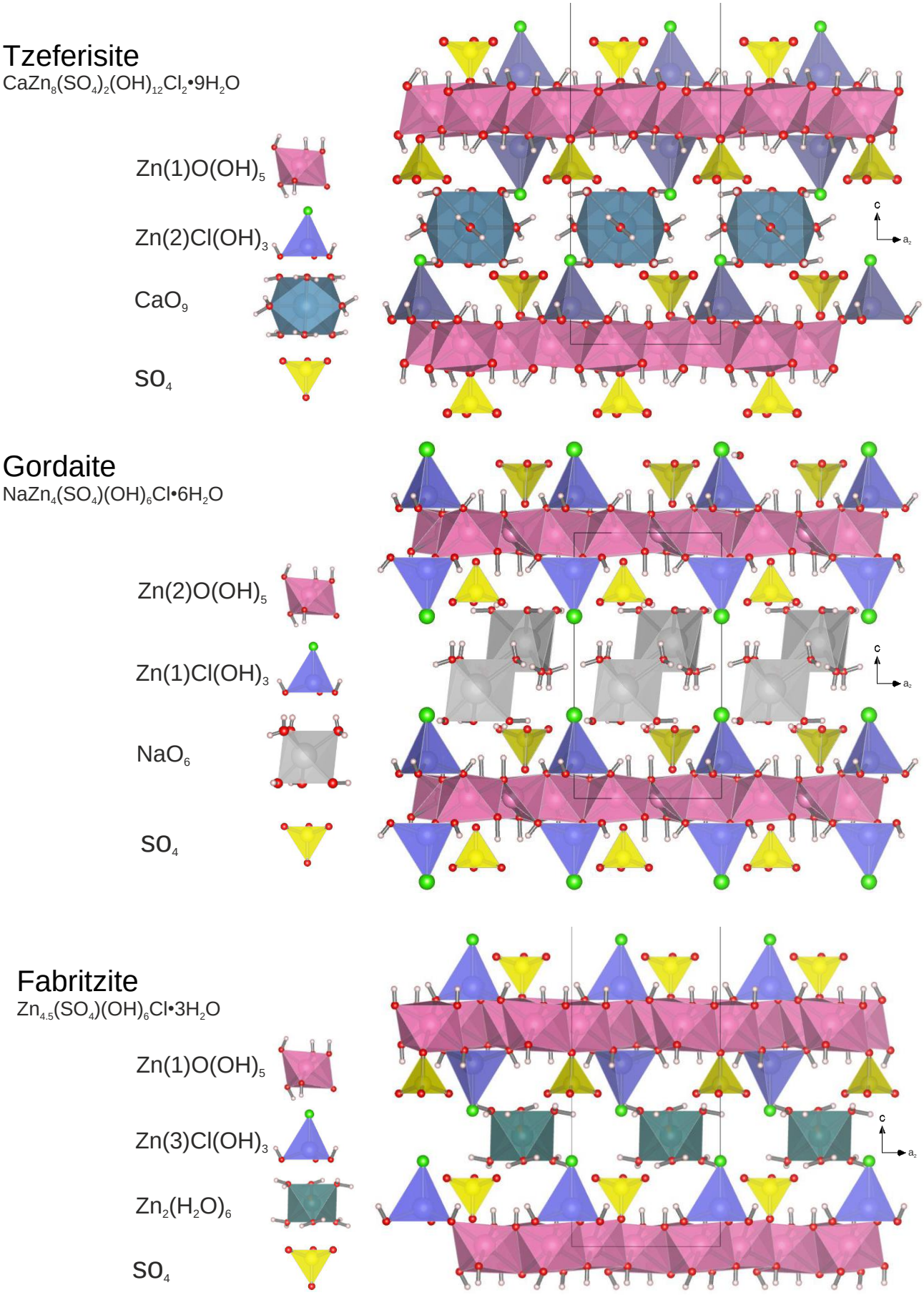

Figure 20. Comparison of the related crystal structure motifs of tzeferisite, gordaite and fabritzite; view of the the brucite–like sheets in projection along [100].

Figures 21a and b show the IR spectra and Raman spectra of the structurally related gordaite $NaZn_4(SO_4)(OH)_6Cl•6H_2O$ compared to tzeferisite. The infrared spectrum of tzeferisite is an absorbance spectrum, that of gordaite is a transmission spectrum (Figure 21a). In the Raman spectra (Figure 21b, spectra offset for clarity), the strongest bands 3470 and 972 cm^{-1} of tzeferesite are visually comparable to gordaite.

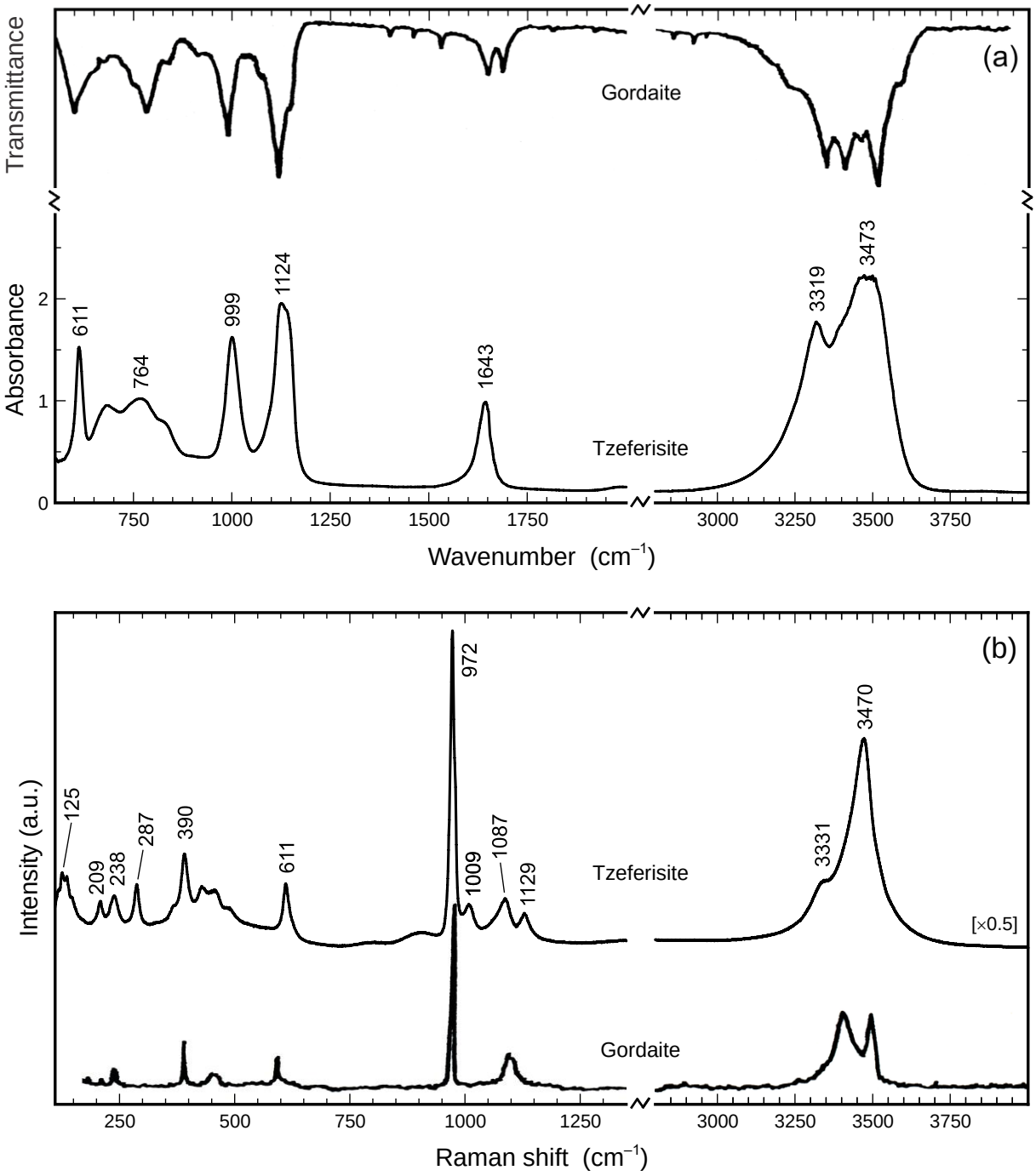

Figure 21. The infrared spectra (a) show tzeferisite in absorbance units and gordaite in transmittance. The Raman spectra (b) give a comparison between the spectra of tzeferisite and gordaite. Unfortunately, the spectra of gordaite were only available in the form of scans by Lutz Nasdala from his study Nasdala et al., 1998.

7. Conclusion

The focus of this work lies on the characterization of three minerals from the Lavrion mining district, i.e. guérinite, bismoclite and the new species tzeferisite.
Guérinite $Ca_6(HAsO_4)_3(AsO_4)_2•10½H_2O$ from the Plaka mine was described with revised formula; it represents a type specimen and should be designated as a neotype and Mine No. 145 as a type locality (Liebhart et. al, 2021).
The occurrence of the rare bismoclite BiOCl from the Jean Baptiste mine in Agios Konstantinos, Attica, also highlights the uniqueness of the Lavrion mining district. The single-crystal X-ray diffraction analysis confirms the crystal structure of the bismuth oxyhalide phase on a natural sample and the Raman spectrum can be useful as a reference for bismoclite.
The new mineral tzeferisite $CaZn_8(SO_4)_2(OH)_{12}Cl_2•9H2O$ from the Ary mine in Dimoliaki, Attica, was studied by single-crystal X-ray diffraction, Raman and infrared spectroscopy. Close structure relationships became evident with the minerals gordaite and fabritzite.

8. List of Figures and Tables

Figure 1. Geological map of Attica, Greece (Boronkay et al., 2021 created with www.geomappapp.org).

Figure 2. Detail of the Plaka mine where guérinite was discovered in April 2019. © Branko Rieck

Figure 3. Locality of bismoclite in the Jean Baptiste mine, April 2014. © Branko Rieck

Figure 4. Spot of tzeferisite in the Ary mine, November 2021. © Branko Rieck

Figure 5. Geological Map of the Cycladic detachment system. WCSD—West Cycladic detachment system from Sifnos to Lavrion, Attica. NCSD—North Cycladic detachment system, NPDS—Naxos-Paros detachments system, and SCDS—South Cycladic detachment system. Inset shows the major active volcanoes (Grasemann et al., 2018).

Figure 6. Guérinite, associated with white, needle-like rauenthalite (lower left) and deformed pharmacolite (right) on calcite matrix that is partially covered by tiny marcasite crystals (mainly left of guérinite) field of view is 3.0 mm. © Branko Rieck

Figure 7. The layer structure of guérinite viewed along the **b** axis. All structure drawings were done with the VESTA software (Momma & Izumi, 2011).

Figure 8. The free molecules O_W10 and O_W11 in the interlayer structure and the hydrogen bonding system (dotted lines) of guérinite.

Figure 9. Linkage scheme of CaO_n polyhedra, AsO_4 and $HAsO_4$ tetrahedra of guérinite.

Figure 10. The layer structure of guérinite along $[10\bar{1}]$.

Figure 11. The layer structure of bismoclite. a) tetragonal antiprisms BiO_4Cl_4 form layers parallel (001), b) ball-and-stick model projected along [010], c) layer structure parallel to (001) (ball-and-stick model compared to representation by polyhedra), and d) respective layers viewed in a projection inclined by 15° illustrating linkage of polyhedra by edges and faces in directions [100] and [010].

Figure 12. Raman spectrum (473 nm excitation) of bismoclite.

Figure 13. Structure of matlockite shown as ball-and-stick and polyhedra model.

Figure 14. Tzeferisite, tiny colourless thin platelets, with associated mineral secondary greenockite on a calcite matrix. © Branko Rieck

Figure 15. Crystal structure of tzeferisite projected parallel to [010].

Figure 16. The infrared spectrum of tzeferisite.

Figure 17. The Raman spectra show the intensity [a.u.] of the Raman shift [cm^{-1}] compared to the measurements at room temperature (RT, see above) and the N_2-cooled sample (–191°C) of tzeferisite.

Figure 18. Raman spectra show the H_2O range comparing RT and N_2 cooling at –191°C based on the measurement of intensity [a.u.] and Raman shift [cm^{-1}] for tzeferisite

Figure 19. Brucite–type sheet of tzeferisite viewed along **c** axis.

Figure 20. Comparison of the related crystal structure motifs of tzeferisite, gordaite and fabritzite; view of the the brucite–like sheets in projection along [100].

Figure 21. The infrared spectra (a) show tzeferisite in absorbance units and gordaite in transmittance. The Raman spectra (b) give a comparison between the spectra of tzeferisite and gordaite. Unfortunately, the spectra of gordaite were only available in the form of scans by Lutz Nasdala from his study Nasdala et al., 1998.

Table 1. Chemical analyses of guérinite [in wt. %].

Table 2. Crystal data and details of the intensity measurement and structure refinement for guérinite.

Table 3. Atom coordinates and displacement parameters with estimated standard deviations [e.s.d.'s] in parentheses for guérinite.

Table 4. Hydrogen bonding scheme [Å, °] for guérinite.

Table 5. Selected interatomic bond distances [Å] and angles [°] for guérinite.

Table 6. Selected bond valence [v.u.] analysis for guérinite.

Table 7. Ideal chemical composition [in wt. %] calculated for different structure proposals of guérinite compared with analytical data.

Table 8. Selected bond valence [v.u.] analysis for guérinite from Catti & Ferraris (1974).

Table 9. Compilation of various minerals and synthetic compounds, chemically related to guérinite.

Table 10. Crystal data and details of the intensity measurement and structure refinement for bismoclite.

Table 11. Atom coordinates and displacement parameters with e.s.d.'s in parentheses for bismoclite. All atoms are on special Wyckoff positions, therefore U^{12}, U^{13} and U^{23} are zero.

Table 12. Selected interatomic bond distances [Å], angles [°] and valences [v.u.] for bismoclite.

Table 13. Compilation of minerals and synthetic compounds, isostructural to bismoclite. Atoms are ordered in the following *AXY* system with
A = Bi^{3+}, Pb^{2+}, Ca^{2+}, Ba^{2+}; *X* = O^{2-}, F^{-}; *Y* = Cl^{-}, F^{-}, OH^{-}.

Table 14. Crystal data and details of the intensity measurement and structure refinement for tzeferisite.

Table 15. Atom coordinates and displacement parameters with e.s.d.'s in parentheses for tzeferisite.

Table 16. Selected interatomic bond distances [Å] and angles [°] for tzeferisite.

Table 17. Bond valence analysis for tzeferisite, calculated within the PLATON program suite (Spek, 2009) by parameters of Brese & O'Keeffe (1991).

Table18. Hydrogen bonding scheme [Å, °] for tzeferisite.

Table 19. Comparison of formula and crystal data of tzeferisite and related minerals and compounds.

Table 20. Selected interatomic angles [°] for guérinite.

Table 21. Comparison of selected interatomic bond distances [Å] of guérinite from Lavrion and published by Catti & Ferraris (1974).

9. References

Adiwidjaja, G., Friese, K., Klaska, K. H. & Schlüter, J. (1997). The crystal structure of gordaite $NaZn_4(SO_4)(OH)_6Cl•6H_2O$. *Zeitschrift für Kristallographie-Crystalline Materials* 212(10), 704–707.

Altherr, R., Kreuzer, H., Wendt, I., Lenz, H., Wagner, G. A., Keller, J., Harre, W. & Höndorf, A. (1982). A late Oligocene/early Miocene high temperature belt in the Attic-Cycladic crystalline complex (SE Pelagonian, Greece). *Geologisches Jahrbuch* 23, 97–164.

Aurivillius, B., Brosset, C., Ledaal, T. & Seip, H. M. (1964). The Crystal Structure of Bismuth Oxide Fluoride. *Acta Chemica Scandinavica*, 18(8).

Avigad, D.,Garfunkel, Z., Jolivet, L. & Azanon, J.M. (1997). Back arc extension and denudation of Mediterranean eclogites. *Tectonics* 16, 924–941.

Baltatzis, E. (1996). Blueschist-to-greenschist transition and the P-T path of prasinites from the Lavrion area, Greece. *Mineralogical Magazine* 60, 551–561.

Bannister, F. A. (1934). The crystal-structure and optical properties of matlockite (PbFCl). *Mineralogical Magazine and Journal of the Mineralogical Society* 24, 49–58.

Bannister, F. A. & Hey, M. H. (1935). *Mineralogical magazine and journal of the Mineralogical Society* 24, 49–58.

Berger, A., Schneider, D. A., Graseman, B. & Stockli, D. (2013). Footwall mineralization during Late Miocene extension along the West Cycladic Detachment System, Lavrion, Greece. *Terra Nova* 25, 181–191.

Bonsall, T. A., Spry, P. G., Voudouris, P., Tombros, S., Seymour, K. & Melfos, V. (2011). The Geochemistry of Carbonate-Replacement Pb-Zn-Ag Mineralization in the Lavrion District, Attica, Greece: Fluid Inclusion, Stable Isotope, and Rare Earth Element Studies. *Economic Geology* 106, 619–651.

Boronkay, K., Stoumpos, G., Benissi, M., Rovolis, G., Korkaris, K., Papastamatiou, D., Dimitriou, G., Chrysikopoulou, A., Miliotis, I., Giakoumis, A., Novack, M. & Marinos, P. (2021). Geological Map of Athens Metropolitan Area, Attica (Greece): A Review Based On Athens Metro Ground Investigation Data. *Bulletin Geological Society of Greece* 57, 68–126.

Brese, N. & O'Keeffe, M. (1991). Bond valence parameters for solids. *Acta Crytallographica Section B–structural Science* 47, 192–197.

Bröcker, M., Bieling, D., Hacker, B. & Gans P. (2004). High-Si phengite records the time of greenschist facies overprinting: implications for models suggesting mega-detachments in the Agean Sea. *Journal of Metamorphic Geology* 22, 427–442.

Bröcker, M. & Keasling, A. (2006). Ion probe U-Pb zircon ages from the high-pressure/low-temperature mélange of Syros, Greece: age diversity and the importance of pre-Eocene subduction. *Journal of Metamorphic Geology* 24, 615–631.

Bruker (2020). APEX3. Bruker AXS Inc., Madison, Wisconsin, USA.

Bunda, S. & Bunda, V. (2013). Raman Spectra of Bismuth Oxyhalide Single Crystals. *Acta Physica Polonica A* 126, 272.

Burns, P., Roberts, A. & Nikischer, A. J. (1998). The crystal structure of $Ca[Zn_8(SO_4)_2(OH)_{12}Cl_2]H_2O_{19}$, a new phase from slag dumps at Val Varenna, Italy. *European Journal of Mineralogy* 10, 923–930.

Catti, M. & Ferraris, G. (1974). Crystal Structure of $Ca_5(HAsO_4)_2(AsO_4)_2•9H_20$ (Guérinite), *Acta Crystallographica Section B* 30, 1789–1794.

Catti, M., Chiari, G. & Ferraris, G. (1980). The structure of ferrarisite, $Ca_5(HAsO_4)_2(AsO_4)_2•9H_2O$, disorder, hydrogen bonding and polymorphism with guerinite. *Bulletin de Minéralogie* 103(5), 541–546.

Catti, M. & Ivaldi, G. (1981). Mechanism of the reaction $Ca_5H_2(AsO_4)_4•9H_2O$ (ferrarisite) → $Ca_5H_2(AsO_4)_4•5H_2O$) (dimorph of vladimirite), and structure of the latter phase. *Zeitschrift für Kristallographie* 157, 119–130.

Catti, M. & Ivaldi, G. (1983). On the Topotactic Dehydration $Ca_3(AsO_4)_2•11H_2O$ (Phaunouxite) → $Ca_3(AsO_4)_2•10H_20$ (Rauenthalite), and the Structures of Both Minerals. *Acta Crystallographica B* 39, 4–10.

Chesnokov, B. V., Nishanbaev, T. P. & Bazhenova, L. F. (1990). Rorisit CaFCl-novyj mineral. *Zapiski Vsesoûznogo mineralogičeskogo obŝestva* 119(3), 73–76.

Chukanov, N. V., Pekov, I. V. & Zadov, A.,E. (2007a). Attikaite, $Ca_3Cu_2Al_2(AsO_4)_4(OH)_4•2H_2O$, a new mineral species. *Geology of Ore Deposits* 49, 720–726.

Chukanov, N. V., Pekov, I.,V., Möckel, S., Mukhanova, A.,A., Belakovsky, D. I., Levitskaya, L. A. & Bekenova, G. K (2010). Kamarizaite, $Fe_3^{+3}(AsO_4)_2(OH)_3•3H_2O$, a new mineral species, arsenate analogue of tinticite. *Geology of Ore Deposits* 52, 599–605.

Chukanov, N. V., Pekov, I. V., Belakovskiy, D. I., Britvin, S. N., Stergiou, V., Voudouris, P. & Magganas, A. (2018). Katerinopoulosite, $(NH_4)_2Zn(SO_4)_2•6H_2O$, a new mineral from the Esperanza mine, Lavrion, Greece. *European Journal of Mineralogy* 30, 821–826.

Chukanov, N. V., Pushcharovsky, D. Y., Zubkova, N. V., Pekov, I. V., Pasero, M., Merlino, S., Möckel, S., Rabadanov, M. K. & Belakovskiy, D. I. (2007b). Zincolivenite $CuZn(AsO_4)(OH)$: A new adamite-group mineral with ordered distribution of Cu and Zn. *Doklady Earth Sciences* 415 A, 841–845.

Coleman, M., Dubosq, R., Schneider, D. A., Grasemann, B. & Soukis, K. (2019). Along-strike consistency of an extensional detachment system, West Cyclades, Greece. *Terra Nova* 31(3), 220–233.

Coleman, M. J., Schneider, D. A., Graseman, B., Soukis, K., Lozios, S. & Hollinetz, M. S. (2020). Lateral termination of a Cycladic-style detachment system (Hymittos, Greece). *Tectonics* 39, e2020TC006128.

Conophagos, C. E. (1980). Le Laurium antique et la technique grecque de la production de l'argent. *Ekdotike Hellados*.

Domeyko, I. (1876). Daubréeite (oxychlorure de bismuth)–espece minerale nouvelle. *Comptes Rendus Hebdomadaires des Seances de 1'Academie des Sciences* 82, 922–923.

Economou, M., Skounakis, S. & Papathanassiou, K. (1981). Magnetite deposits of skarn type from the Plaka area of Laurium, Greece. *Chemie der Erde* 40, 241–252.

Ferraris, G. (1969). The crystal structure of pharmacolite, $CaH(AsO_4)_2 \cdot H_2O$. *Acta Crystallographica Section B: Structural Crystallography and Crystal Chemistry*, 25(8), 1544–1550.

Ferraris, G. & Abbona, F. (1972). The crystal structure of $Ca_5(HAsO_4)_2(AsO_4)_2 \cdot 4H_2O$ (Sainfeldite). *Bulletin de la Société française de Minéralogie et de Cristallographie* 95, 1. *Acta Crystallographica B* 25, 1544.

Ferraris, G. & Chiari, G. (1969). The Crystal Structure of $CaHAsO_4$ (Weilite). *Acta Crystallographica B* 26, 403.

Ferraris, G., Jones, D. W. & Yerkess, J. (1971). A Neutron and X-ray Refinement of the Crystal Structure of $CaHAsO_4 \cdot H_20$ (Haidingerite). *Acta Crystallographica B* 28, 209.

Forster, M. A. & Lister G. S. (2005). Several-distinct tectono-metamorphic slices in the Cycladic eclogite-blueschist belt, Greece. *Contributions to Mineralogy and Petrology* 150, 523–545.

Gaines, R. V., Skinner, H. C. W., Foord, E. E., Mason, B. & Rosenzweig, A. (1998). Dana's New Mineralogy. *Journal of the American Chemical Society* 120(11), 2693.

Galy, J., Meunier, G., Andersson, S. & Åström, A. (1975). Stéréochimie des Eléments Comportant des Paires Non Liées: Ge (II), As (III), Se (IV), Br (V), Sn (II), Sb (III), Te (IV), I (V), Xe (VI), Tl (I), Pb (II), et Bi (III)(Oxydes, Fluorures et Oxyfluorures). *Journal of Solid State Chemistry* 13(1-2), 142–159.

Gautier, P. & Brun, J. P. (1994). Crustal-scale geometry and kinematics of late-orogenic extension in the central Aegean (Cyclades and Evvia Island). *Tectonophysics* 238, 399–424.

Giester, G. & Rieck, B. (1995). Mereiterite, $K_2Fe[SO_4]_2 \cdot 4H_2O$, a new leonite-type mineral from the Lavrion Mining District, Greece. *European Journal of Mineralogy* 7, 559–566.

Giester, G. & Rieck, B. (2010). Drobecite, a novel mineral from the Lavrion, Greece, deposit. *In Proceedings of the 20th General Meeting of IMA*, 21–27.

Giester, G., Rieck, B. & Brandstätter, F. (1998). Niedermayrite, $CdCu_4[(OH)_6(SO_4)_2] \cdot 4H_2O$, a new mineral from the Lavrion mining district, Greece. *Mineralogy and Petrology* 63, 19–34.

Grasemann, B., Schneider, D. A., Stöckli, D. F., & Iglseder, C. (2012). Miocene bivergent crustal extension in the Aegean: Evidence from the western Cyclades (Greece). *Lithosphere* 4, 23–39.

Grasemann, B., Huet, B., Schneider, D. A., Rice, A. H. N., Lemonnier, N. & Tschegg, C. (2018). Miocene postorogenic extension of the Eocene synorogenic imbricated Hellenic subduction channel: New constraints from Milos (Cyclades, Greece). *The geological society of America* 130, 238–262.

Hübschle, C. B., Sheldrick, G. M. & Dittrich, B. (2011). ShelXle: a Qt graphical user interface for SHELXL. *Journal of Applied Crystallography* 44, 1281–1284

Jolivet, L. & Brun, J. P. (2010). Cenozoic geodynamic evolution of the Aegean. *International Journal of Earth Sciences* 99, 109–138.

Jolivet, L., Faccenna, C., Goffé, B., Burov, E. & Acard, F. (2003). Subduction tectonics and exhumation of high-pressure metamorphic rocks in the Mediterranean orogens. *American Journal of Science* 303, 353–409.

Jolivet, L., Faccenna, C., Huet, B., Labrousse, L., Le Pourhiet, L., Lacombe, O., Lecomte, E., Burov, E., Denèle, Y., Brun, J.–P., Philippon, M., Paul, A., Salaün, G., Karabulut, H., Piromallo, C., Monié, P., Gueydan, F., Okay, A. I., Oberhänsli, R., Pourteau, A., Augier, R., Gadenne, L., & Driussi, O. (2013). Aegean tectonics: Strain localization, slab tearing and trench retreat. *Tectonophysics* 597, 1–33.

Katsikatsos, G. (1977). La structure tectonique d´Attique et de l´lle d´Eubée. *Colloquium on the Aegean region* 1, 211–220.

Katsikatsos, G., Migiros, G., Triantaphyllis M. & Mettos, A. (1986). Geological structure of internal Hellenides. *Geological and geophysical research*,191–212.

Keramidas, K. G., Voutsas, G. P. & Rentzeperis, P. I. (1993). The crystal structure of BiOCl. *Zeitschrift für Kristallographie* 205, 35–40.

Kokkoros, P. (1950). Ktenasit, ein Zink-Kupfersulfat aus Lavrion (Griechenland). *Mineralogy and Petrology* 1(4), 342–346.

Kolitsch, U. & Giester, G. (2013). The crystal structure of a new secondary zinc mineral from Lavrion, Greece: $Zn_9(SO_4)_2(OH)_{12}Cl•6H_2O$. *Mitteilungen Österreichischen Mineralogischen Gesellschaft* 159, 74.

Kolitsch, U., Rieck, B., Topa, D., Giester, G. & Zeug, M. 2023. Fabritzite, IMA 2020-040, in: CNMNC Newsletter 71, *European Journal of Mineralogy* 35.

Kolitsch, U., Rieck, B. & Voudouris, P. (2015). Mineralogy and genesis of the Lavrion ore deposit: New insights from the study of ore and accessory minerals. *Mitteillung der Österreichisch Mineralogischen Gesellschaft* 161, 66.

Krause, W., Bernhardt, H.-J., Braithwaite, R. S. W., Kolitsch, U. & Pritchard, R. (2006). Kapellasite, $Cu_3Zn(OH)_6Cl_2$, a new mineral from Lavrion, Greece. *Mineralogical Magazine* 70, 329–340.

Kruckenberg, S. C., Vanderhaeghe, O., Ferré, E. C., Teyssier, C. & Whitney, D. L. (2011). Flow of partially molten crust and the internal dynamics of a migmatite dome, Naxos, Greece. *Tectonics* 30, TC3001.

Kulikov, I. V., Devyatov, V. E. & Gromov, A. V. (1982). On a new natural compound: Calcium fluoride chloride. Izvestiya Vysshikh Uchebnykh Zavedenii. *Geologiya i Razvedka* 25, 120–122.

Leleu, M. & Neumann, M. (1969). L´âge des formations d´Attique (Grèce): du Paléozoïque au Mésozoïque. *Comptes rendus de l'Académie des sciences* 268, 1361–1363.

Leleu, M., Morikis, A. & Picot, P. (1973). Sur des mineralisations de type skarn au Laurium (Grèce). *Mineralium Deposita* 36, 477–489.

Liebhart, I., Rieck, B. & Giester, G. (2021). Contributions to the crystal structure of guérinite from the Lavrion mining district, Greece. *Mitteilungen der Österreichischen Mineralogischen Gesellschaft* 167, 124.

Liebich, B. W. & Nicollin, D. (1977). Refinement of the PbFCl types BaFI, BaFBr and CaFCl. *Acta Crystallographica Section B*: *Structural Crystallography and Crystal Chemistry* 33(9), 2790–2794.

Lister, G. S.; Banga, G. & Feenstra, A. (1984). Metamorphic core complex of Cordilleran type in the Cyclades, Aegean Sea, Greece. *Geology* 12, 221–225.

Lekkas, S., Skourtsos, E., Soukis, K., Kranis, H., Lozios, S., Alexopoulos, A. & Koutsovitsis, P. (2011). Late Miocene detachment faulting and crustal extension in SE Attica (Greece). *In Geophysical Research Abstracts* 13, EGU2011-13016.

Marakis, G. (1968). Remarks on the age of sulfide mineralization in Cyclades area. *Annales Géologiques des Pays Helléniques* 19, 695–700.

Marinos, G. & Petrascheck, W. E. (1956). Laurium: Geological and geophysical research. Greece. *Institute for Geology and Subsurface Research* 5, 266.

Marinos, G., Katsikatsos, G., Mercier, J., Vergely, P., Aubouin, J., Symeonidis, N. & Marcopoulou-Diacantoni, A. (1977). Réunion extraordinaire de la Soc. Géol. Grèce en Eubée et en Attique*. Bulletin de la Société Géologique de France* 19(1), 103–116.

Momma, K. & Izumi, F. (2011). "VESTA 3 for three-dimensional visualization of crystal, volumetric and morphology data," Journal of Applied Crystallography 44, 1272–1276.

Mountain, E. D. (1935). Two new bismuth minerals from South Africa. *Mineralogical magazine and journal of the Mineralogical Society* 24, 59–64.

Nasdala, L., Witzke, T., Ullrich, B. & Brett, R. (1998). Gordaite [$Zn_4Na(OH)_6(SO_4)Cl_6 \bullet H_2O$]: Second occurrence in the Juan de Fuca Ridge, and new data. *American Mineralogist* 83(9-10), 1111–1116.

Nefedov, E. I. (1961). Guérinite, a new mineral*. Materialy Vses Nauchno-Issled Geology Institution* 45(2), 113–115.

Olds, T., Kampf, A., Dal Bo, F., Burns, P. C., Guo, X. & McCloy, J. S. (2020). Jeankempite, $Ca_5(AsO_4)_2(AsO_3OH)_2(H_2O)_7$, a new arsenate mineral from the Mohawk Mine, Keweenaw County, Michigan, USA. *Mineralogical Magazine* 84, 959–969.

Ondruš, P., Skála, R., Plášil, J., Sejkora, J., Veselovský, F., Čejka, J. & Lapčák, L. (2013). Švenekite, $Ca[AsO_2(OH)_2]_2$, a new mineral from Jáchymov, Czech Republic. *Mineralogical Magazine*, *77*(6), 2711–2724.

Orgel, L. E. (1959). 769. The stereochemistry of B subgroup metals. Part II. The inert pair. *Journal of the Chemical Society (Resumed)*, 3815–3819.

Papanikolaou, D. J. (1987). Tectonic evolution of the Cycladic blueschist belt (Aegean Sea, Greece). *NATO ASI series* 218, 429–450.

Pasero, M., & Perchiazzi, N. (1996). Crystal structure refinement of matlockite. *Mineralogical Magazine* 60(402), 833–836.

Pekov, I. V., Chukanov, N. V., Zadov, A.E., Voudouris, P., Magganas, A. & Katerinopoulos, A. (2011). Agardite-(Nd) $NdCu_6(AsO_4)_3(OH)_6•3H_2O$ from the Hilarion Mine, Lavrion, Greece: Mineral description and chemical relations with other members of the agardite-zálesiite solid-solution system. *Journal of Geosciences* 57, 249–255.

Pekov, I. V. Chukanov, N. V., Yapaskurt, V. O., Rusakov, V. S., Belakovskiy, D. I., Turchkova, A. G., Voudouris, P., Magganas, A. & Katerinopoulos, A. (2013). Hilarionite, $Fe^{3+}_2(SO_4)(AsO_4)(OH)•6H_2O$, a new supergene mineral from Lavrion, Greece. *Geology of Ore Deposits* 56, 567–575.

Pekov, I. V., Chukanov, N. V., Varlamov, D. A., Belakovskiy, D. I., Turchkova, A. G., Voudouris, P., Katerinopoulos, A. & Magganas, A. (2016). Nickeltsumcorite, $Pb(Ni,Fe^{3+})_2(AsO_4)_2•(H_2O,OH)_2$, a new tsumcorite-group mineral from Lavrion, Greece. *Mineralogical Magazine* 80, 337–346.

Photiades, A. (2003). Geological structure of the Lavreotiki area (Attica, Greece*). Lavreotiki Excursion Guide*, 24–28.

Photiades, A. & Carras, N. (2001). Stratigraphy and geological structure of the Lavrion area (Attica, Greece). *Bulletin of the Geological* 34, 103–109.

Photiades, A. & Saccani, E. (2006). Geochemistry and tectono-magmatic significance of HP/LT metaophiolites of the Attic-Cycladic zone in the Lavrion area (Attica, Greece). *Ofioliti* 31, 89–102.

Pierrot, R. (1964). Contribution á la mindéralogie des arséniates calciques et calcomagnésiens naturels. *Bulletin de Minéralogie* 87, 169–211.

Reinecke, T., Altherr, R., Hartung, B., Hatzipanagiotou, K., Kreuzer, H., Harre, W., Klein, H., Keller, J., Geenen, E. & Boeger, H. (1982). Remnants of a Late Cretaceous high temperature belt on the island of Anafi (Cyclades, Greece). *Neues Jahrbuch für Mineralogie Abhandlungen* 145, 157–182.

Rieck, B. (2012). Neue Minerale aus dem Lagerstätten-Bezirk Lavrion, Griechenland und den Kalahari Mangan Feldern, Republik Südafrika. Print.

Rieck, B., Giester, G., Lengauer, C. & Nasdala, L. (2020). Katsarosite. *European Journal of Mineralogy* 32, 495.

Rieck, B., Giester, G., Lengauer, L. C., Chanmuang, C. N. & Topa, D. (2020). Stergiouite, $CaZn_2(AsO_4)_2•4H_2O$ - A new mineral from the Lavrion Mining District, Greece*. Mineralogy and Petrology* 114, 319–327.

Rieck, B., Kolitsch, U., Voudouris, P., Giester, G. & Tzeferis, P. (2018). Weitere Neufunde aus Lavrion, Griechenland. *Mineralien-Welt* 29(5), 32–77.

Rieck, B., Kolitsch, U., Voudouris, P., Giester, G. & Tzeferis, P. (2020). Lavrion, Griechenland: Weitere Neufunde aus dem berühmten Bergbaurevier. *Mineralien–Welt* 31(3), 6–21.

Rieck, B., Kolitsch, U., Voudouris, P., Giester, G. & Tzeferis, P. (2022). Neubestimmung aus dem Bergbaubezirk Lavrion, Griechenland. *Mineralien–Welt* 33(5), 6–20.

Rieck, B., Lengauer, C. L. & Giester, G. (2019). Voudourisite, $Cd(SO_4)\cdot H_2O$, and lazaridisite, $Cd_3(SO_4)_3\bullet 8H_2O$, two new minerals from the Lavrion Mining District, Greece. *Mineralogical Magazine* 83, 551–559.

Rieck, B., Liebhart, I., Giester, G., Libowitzky, E., Chanmuang, N. C., and Kolitsch, U. (2023). Tzeferisite, IMA 2022-094, in: CNMNC Newsletter 71. *European Journal of Mineralogy* 35.

Rieck, B. & Rieck, P. (1999). Silber, Arsen und Antimon: Vererzungen im Revier Plaka (Teil II). *Lapis* 24(7/8), 59–63.

Ring, U., Glodny, J., Will, T. & Thomson, S. (2010). The Hellenic subduction system: High-pressure metamorphism, exhumation, normal faulting, and large-scale extension. *Annual Review of Earth Planet* 38, 45–76.

Ring, U. & Layer, P. W. (2003). High-pressure metamorphism in the Aegean, eastern Mediterranean: Underplating and exhumation from the Late Cretaceous until the Miocene to Recent above the retreating Hellenic subduction zone. *Tectonics* 22(3), 23–46.

Ross, J., Voudouris, P., Melfos, V., Vaxevanopoulos, M., Soukis, K. & Merigot, K. (2021). What did the ancient Greeks mine at Lavrion and when did they mine it? *Geoarchaeology* 36, 617–642.

Sauvage, M. (1974). Refinement of the structures of SrFCl and BaFCl. *Acta Crystallographica Section B: Structural Crystallography and Crystal Chemistry* 30(11), 2786–2787.

Scheffer, C., Vanderhaeghe, O., Lanari, P., Tarantola, A., Ponthus, L., Photiades, A. & France, L. (2016). Syn- to post-orogenic exhumation of metamorphic nappes: Structure and thermobarometry of the western Attic-Cycladic metamorphic complex (Lavrion, Greece). *Journal of Geodynamics* 96, 174–193.

Scheffer, C., Tarantola, A., Vanderhaeghe, O., Voudouris, P., Rigaudier, T., Photiadis, A., Morin, D. & Alloucherie, A. (2017). The Lavrion Pb-Zn-Fe-Cu-Ag detachment-related district (Attica, Greece): Structural control on hydrothermal flow and element transfer-deposition. *Tectonophysics* 717, 607–627.

Scheffer, C., Tarantola, A., Vanderhaeghe, O., Voudouris, P., Spry, P. G., Rigaudier, T. & Photiades, A. (2019). The Lavrion Pb-Zn-Ag-rich Vein and Breccia Detachment-Related Deposits (Greece): Involvement of Evaporated Seawater and Meteoric Fluids during Post-Orogenic Exhumation. *Economic Geology* 114, 1415–1442.

Seman, S., Soukis, K., Stockli, D. F., Skourtsos, E., Kranis, H., Lozios, S., & Shin, T. (2013, April). Provenance of metasediments and Miocene exhumation history of the Lavrion Peninsula, South Attica, Greece: a combined structural,(U-Th)/He, and detrital zircon U-Pb study. In *EGU General Assembly Conference Abstracts* (pp. EGU2013-12605).

Seman, S., Stockli, D. F. & Soukis, K. (2017). The provenance and internal structure of the Cycladic Blueschist Unit revealed by detrital zircon geochronology, Western Cyclades, Greece. *Tectonics* 36, 1407–1429.

Sheldrick G.M. (2018/3). A short history of SHELX. *Acta Crystallographica* 64A, 112–122.

Shimazaki, H., Miyawaki, R., Yokoyama, K., Matsubara, S. & Yang, Z. (2008). Zhangpeishanite, BaFCl, a new mineral in fluorite from Bayan Obo, Inner Mongolia, China. *European Journal of Mineralogy* 20(6), 1141–1144.

Skarpelis, N. (2007).The Lavrion deposit (SE Attica, Greece): Geology, mineralogy and minor elements chemistry. *Neues Jahrbuch fur Mineralogie-Abhandlungen* 83, 227–249.

Skarpelis, N. & Argyraki, A. (2009). Geology and origin of supergene ore at the Lavrion Pb-Ag-Zn deposit, Attica, Greece. *Resource geology* 59(1), 1–14.

Spek, A. L. (2009). Structure validation in chemical crystallography. *Acta Crystallographica D* 65, 148–155.

Tarantola, A., Scheffer, C., Vanderhaeghe, O., Voudouris, P., Photiades, A. & Morin, D. (2021). Geologic and metallogenic overview of the Lavrion mining district: A guide for archaeological exploration. *Der Anschnitt*, in press.

Testa, F. J., Cooke, D. R., Zhang, L., & Mas, G. R. (2016). Bismoclite (BiOCl) in the San Francisco de los Andes Bi–Cu–Au Deposit, Argentina. First Occurrence of a Bismuth Oxychloride in a Magmatic–Hydrothermal Breccia Pipe and Its Usefulness as an Indicator Phase in Mineral Exploration. *Minerals* 6(3), 62.

Voudouris, P. & Economou-Eliopoulos, M. (2003). Mineralogy and chemistry of Cu-rich ores from the Kamariza carbonate-hosted deposit (Lavrion), Greece. *Mineral Exploration and Sustainable Development* 499–502.

Voudouris, P., Mavrogonatos, C., Rieck, B., Kolitsch, U., Spry, P. G., Scheffer, C., Tarantola, A., Vanderhaeghe, O., Galanos, E., Melfos, V., Zaimis, S., Soukis, K. & Photiades, A. (2018). The Gersdorffite-Bismuthinite-Native Gold Association and the Skarn-Porphyry Mineralization in the Kamariza Mining District, Lavrion, Greece. *Minerals* 8, 531.

Voudouris, P., Melfos, V., Spry, P. G., Bonsall, T., Tarkian, M. & Economou-Eliopoulos, M. (2008a). Mineralogical and fluid inclusion constraints on the evolution of the Plaka intrusion-related ore system, Lavrion, Greece. *Mineralogy and Petrology* 93, 79–110.

Voudouris, P., Melfos, V., Spry, P. G., Bonsall, T. A., Tarkian, M., & Solomos, C. (2008b). Carbonate-replacement Pb–Zn–Ag±Au mineralization in the Kamariza area, Lavrion, Greece: Mineralogy and thermochemical conditions of formation. *Mineralogy and Petrology* 94, 85–106.

Voudouris, P., Melfos, V., Mavrogonatos, C., Photiades, A., Moraiti, E., Rieck, B., Kolitsch, U., Tarantola, A., Scheffer, C., Morin, D., Vanderhaeghe, O., Spry, I., Ross, J., Soukis, K., Vaxevanopoulos, M., Pekov, I., Chukanov, N. V., Magganas, A., Kati, M., Katerinopoulos, A. & Zaimis, S. (2021). The Lavrion Mines: A Unique Site of Geological and Mineralogical Heritage. *Minerals* 11, 76.

Weil, M., & Kubel, F. (2001). Matlockite-type PbFI. *Acta Crystallographica Section E*: *Structure Reports Online*, 57(9), i80–i81.

Wendel, W. & Rieck, B. (1999a). Die wichtigsten Mineralfundstellen Lavrions. *Lapis* 24(7/8), 25–33.

Wendel, W. & Rieck, B. (1999b). Silber, Arsen und Antimon: Vererzungen im Revier Plaka (Teil I). *Lapis* 24(7/8), 53–58.

Wind, S. C., Schneider, D. A., Hannington, M. D. & McFarlane, C. R. M. (2020). Regional similarities in lead isotopes and trace elements in galena of the Cyclades Mineral District, Greece with implications for the underlying basement. *Lithos* 366, 1–27.

Yang, H., Evans, S. H., Downs, T. & Jenkins R. A. (2011). The crystal structure of vladimirite, with a revised chemical formula, $Ca_4(AsO_4)_2(AsO_3OH)•4H_2O$. *The Canadian Mineralogist* 49, 1055–1064.

Yatimov, U. A., Belogub, E. V., Shilovskikh, V. V., & Blinov, I. A. (2022). Zavaritskite from Sulfide–Magnetite Ore of the Aktash Skarn Deposit, Western Karamazar. *Geology of Ore Deposits* 64(7), 513–518.

Zhu, L., Seff, K., Witzke, T. & Nasdala, L. (1997). Crystal structure of $Zn_4Na(OH)_6SO_4Cl•6H_2O$. *Journal of Chemical Crystallography* 27, 325–329.

10. Appendix

Table 20. Selected interatomic angles [°] for guérinite.

O1-As1-O2	109.57 (16)	O5-As2-O7	107.43 (13)	O9-As3-O10	110.95 (13)
O1-As1-O3	104.89 (14)	O6-As2-O5	111.05 (13)	O9-As3-O11	107.73 (14)
O1-As1-O4	117.33 (15)	O6-As2-O7	103.79 (13)	O9-As3-O12	112.09 (13)
O3-As1-O2	110.12 (16)	O6-As2-O8	111.69 (13)	O11-As3-O10	111.61 (13)
O4-As1-O2	101.63 (16)	O8-As2-O5	112.57 (13)	O11-As3-O12	112.10 (13)
O4-As1-O3	113.28 (15)	O8-As2-O7	109.84 (13)	O12-As3-O10	102.38 (13)
O–As1–O	101.6 - 117.3	O–As2–O	103.8 - 112.6	O–As3–O	102.4 - 112.1

O13-As4-O14	106.18 (13)	O17-As5-O18	109.13 (16)
O13-As4-O15	113.57 (13)	O17-As5-O20	108.00 (17)
O15-As4-O14	101.53 (13)	O19-As5-O17	112.90 (17)
O16-As4-O13	113.79 (13)	O19-As5-O18	107.32 (17)
O16-As4-O14	109.56 (13)	O19-As5-O20	113.62 (17)
O16-As4-O15	111.30 (14)	O20-As5-O18	105.54 (16)
O–As4–O	101.5 - 113.8	O–As5–O	105.6 - 113.6

O4–Ca1–O15	82.72 (10)	O6–Ca2–O13	124.04 (10)	O7–Ca3–O10	86.13 (9)
O4–Ca1–O3	154.79 (11)	O6–Ca2–O16	145.39 (10)	O7–Ca3–O5	154.37 (10)
O4–Ca1–O16	125.30 (10)	O6–Ca2–O13	75.65 (9)	O7–Ca3–O20	71.33 (9)
O4–Ca1–O_w3	80.60 (12)	O6–Ca2–O3	81.19 (9)	O7–Ca3–O10	125.09 (9)
O4–Ca1–O7	112.79 (9)	O6–Ca2–O_w1	78.22 (9)	O7–Ca3–O_w1	80.60 (9)
O4–Ca1–O6	74.64 (10)	O6–Ca2–O_w2	112.76 (10)	O7–Ca3–O3	75.17 (9)
O15–Ca1–O3	87.09 (10)	O13–Ca2–O16	80.25 (9)	O7–Ca3–O17	127.94 (9)
O15–Ca1–O16	84.48 (9)	O13–Ca2–O13	71.69 (9)	O10–Ca3–O5	78.94 (9)
O15–Ca1–O_w3	105.84 (14)	O13–Ca2–O3	88.92 (9)	O10–Ca3–O20	101.84 (10)
O15–Ca1–O7	163.83 (10)	O13–Ca2–O_w1	151.82 (9)	O10–Ca3–O1	145.18 (9)
O15–Ca1–O6	128.25 (9)	O13–Ca2–O_w2	97.09 (10)	O10–Ca3–O_w1	81.90 (9)
O3–Ca1–O16	76.20 (9)	O16–Ca2–O13	138.84 (9)	O10–Ca3–O3	150.93 (9)
O3–Ca1–O_w3	80.12 (12)	O16–Ca2–O3	74.53 (9)	O10–Ca3–O17	83.18 (9)
O3–Ca1–O7	76.87 (9)	O16–Ca2–O_w1	72.59 (9)	O5–Ca3–O20	131.97 (10)
O3–Ca1–O6	128.73 (9)	O16–Ca2–O_w2	84.60 (10)	O5–Ca3–O1	76.27 (9)
O16–Ca1–O_w3	153.64 (11)	O13–Ca2–O3	132.62 (10)	O5–Ca3–O_w1	76.78 (9)
O16–Ca1–O7	89.68 (9)	O13–Ca2–O_w1	135.21 (9)	O5–Ca3–O3	109.12 (9)
O16–Ca1–O6	72.71 (9)	O13–Ca2–O_w2	70.08 (10)	O5–Ca3–O17	71.08 (9)
O_w3–Ca1–O7	73.67 (12)	O3–Ca2–O_w1	76.94 (9)	O20–Ca3–O1	77.88 (10)
O_w3–Ca1–O6	115.17 (14)	O3–Ca2–O_w2	157.00 (10)	O20–Ca3–O_w1	151.24 (10)
O7–Ca1–O6	63.40 (8)	O_w1–Ca2–O_w2	87.80 (10)	O20–Ca3–O3	93.13 (10)
O–Ca1–O	63.4 - 163.8	O–Ca2–O	70.1 - 157.0	O20–Ca3–O17	61.53 (9)
				O1–Ca3–O_w1	115.18 (9)
O11–Ca4–O1	150.28 (11)	O8–Ca5–O5	166.04 (10)	O1–Ca3–O3	62.19 (8)
O11–Ca4–O_w4	108.75 (16)	O8–Ca5–O12	102.94 (9)	O1–Ca3–O17	65.88 (9)
O11–Ca4–O7	87.98 (9)	O8–Ca5–O_w5	79.80 (10)	O_w1–Ca3–O3	73.35 (8)
O11–Ca4–O17	86.17 (10)	O8–Ca5–O10	87.77 (9)	O_w1–Ca3–O17	146.57 (9)
O11–Ca4–O20	77.59 (10)	O8–Ca5–O12	93.55 (9)	O3–Ca3–O17	125.88 (9)
O11–Ca4–O5	79.06 (9)	O8–Ca5–O10	86.80 (9)	O–Ca3–O	62.2 - 154.4
O1–Ca4–O_w4	92.32 (15)	O5–Ca5–O12	86.42 (9)		
O1–Ca4–O7	87.23 (10)	O5–Ca5–O_w5	91.58 (10)	O9–Ca6–O14	73.30 (9)

O1–Ca4–O17	76.13 (11)	O5–Ca5–O10	79.61 (9)	O9–Ca6–O_w2	110.90 (11)
O1–Ca4–O20	127.69 (10)	O5–Ca5–O12	88.74 (9)	O9–Ca6–O_w6	163.02 (12)
O1–Ca4–O5	72.74 (9)	O5–Ca5–O10	106.29 (9)	O9–Ca6–O_w7	85.85 (13)
O_w4–Ca4–O7	142.96 (15)	O12–Ca5–O_w5	81.44 (10)	O9–Ca6–O_w8	86.64 (16)
O_w4–Ca4–O17	81.71 (14)	O12–Ca5–O10	154.42 (10)	O9–Ca6–O_w9	113.06 (16)
O_w4–Ca4–O20	80.88 (13)	O12–Ca5–O12	127.36 (8)	O14–Ca6–O_w2	75.82 (10)
O_w4–Ca4–O5	151.34 (12)	O12–Ca5–O10	70.24 (8)	O14–Ca6–O_w9	69.01 (12)
O7–Ca4–O17	133.50 (11)	O_w5–Ca5–O10	77.66 (10)	O_w8–Ca6–O14	130.13 (22)
O7–Ca4–O20	70.52 (9)	O_w5–Ca5–O12	151.13 (10)	O_w8–Ca6–O_w2	153.14 (21)
O7–Ca4–O5	62.46 (8)	O_w5–Ca5–O10	145.01 (9)	O_w8–Ca6–O_w6	81.37 (19)
O17–Ca4–O20	150.87 (11)	O10–Ca5–O12	74.01 (9)	O_w8–Ca6–O_w7	84.41 (25)
O17–Ca4–O5	71.14 (10)	O10–Ca5–O10	134.28 (8)	O_w8–Ca6–O_w9	78.56 (21)
O20–Ca4–O5	127.66 (9)	O12–Ca5–O10	61.11 (8)	O_w7–Ca6–O14	136.71 (16)
O–Ca4–O	62.5 - 151.3	O–Ca5-O	61.1 - 166.0	O_w7–Ca6–O_w2	77.06 (15)
				O_w7–Ca6–O_w6	81.07 (16)
				O_w7–Ca6–O_w9	153.43 (17)
				O_w6–Ca6–O14	123.68 (12)
				O_w6–Ca6–O_w2	76.71 (14)
				O_w6–Ca6–O_w9	76.35 (18)
				O_w2–Ca6–O_w9	110.58 (15)
				O–Ca6–O	73.3 - 163.0

Table 21. Comparison of selected interatomic bond distances [Å] of guérinite from Lavrion and published by Catti & Ferraris (1974).

	Guérinite from Laurion mining district	Guérinite by Catti & Ferraris, 1974
As1-O1	1.654 (3)	1.65
As1-O2	1.733 (3)	1.69
As1-O3	1.688 (3)	1.75
As1-O4	1.661 (3)	1.67
<As1$^{[4]}$-O>	<1.684>	<1.69>
As2-O5	1.684 (2)	1.65
As2-O6	1.666 (2)	1.62
As2-O7	1.697 (3)	1.66
As2-O8	1.679 (3)	1.51
<As2$^{[4]}$-O>	<1.682>	<1.61>
As3-O9	1.667 (3)	1.69
As3-O10	1.697 (3)	1.65
As3-O11	1.684 (3)	1.57
As3-O12	1.694 (3)	1.59
<As3$^{[4]}$-O>	<1.686>	<1.63>
As4-O13	1.665 (3)	1.70
As4-O14	1.755 (3)	1.75
As4-O15	1.675 (3)	1.75
As4-O16	1.663 (3)	1.58
<As4$^{[4]}$-O>	<1.690>	<1.69>

As5-O17	1.668 (3)	1.67
As5-O18	1.737 (3)	1.79
As5-O19	1.666 (3)	1.67
As5-O20	1.679 (3)	1.66
<As5[4]-O>	<1.688>	<1.69>
Ca1-O3	2.375 (3)	2.31
Ca1-O4	2.348 (3)	2.32
Ca1-O6	2.558 (3)	2.48
Ca1-O7	2.478 (3)	2.45
Ca1-O15	2.365 (3)	2.34
Ca1-O16	2.396 (3)	2.47
Ca1-O_w3	2.449 (4)	2.46
<Ca1[7]-O>	<2.424>	<2.40>
Ca2-O3	2.459 (3)	2.551
Ca2-O6	2.285 (3)	2.38
Ca2-O13	2.322 (3)	2.42
Ca2-O13	2.431 (3)	2.32
Ca2-O16	2.402 (3)	2.47
Ca2-O_w1	2.462 (3)	2.55
Ca2-O_w2	2.496 (3)	2.43
<Ca2[7]-O>	<2.408>	<2.44>
Ca3-O1	2.555 (3)	2.48
Ca3-O3	2.564 (3)	2.51
Ca3-O5	2.412 (3)	2.43
Ca3-O7	2.378 (3)	2.37
Ca3-O10	2.411 (3)	2.41
Ca3-O17	2.815 (4)	2.87
Ca3-O20	2.441 (3)	2.54
Ca3-O_w1	2.562 (3)	2.53
<Ca3[8]-O>	<2.517>	<2.52>
Ca4-O1	2.328 (3)	2.40
Ca4-O5	2.806 (3)	2.83
Ca4-O7	2.409 (3)	2.51
Ca4-O11	2.317 (3)	2.38
Ca4-O17	2.419 (3)	2.47
Ca4-O20	2.458 (3)	2.56
Ca4-O_w4	2.371 (4)	2.37
<Ca4[7]-O>	<2.444>	<2.50>
Ca5-O5	2.343 (3)	2.37
Ca5-O8	2.342 (3)	2.46
Ca5-O10	2.444 (3)	2.75
Ca5-O10	2.727 (3)	2.50
Ca5-O12	2.367 (3)	2.54
Ca5-O12	2.450 (3)	2.42
Ca5-O_w5	2.431 (3)	2.54
<Ca5[7]-O>	<2.443>	<2.51>

Ca6-O9	2.270 (3)	2.24
Ca6-O14	2.494 (3)	2.53
Ca6-O_w2	2.507 (3)	2.56
Ca6-O_w6	2.410 (4)	2.40
Ca6-O_w7	2.391 (4)	2.37
Ca6-O_w8	2.363 (5)	2.46
Ca6-O_w9	2.514 (5)	2.58
<$Ca6^{[7]}$-O>	<2.421>	<2.45>

Abstract (english)

The Lavrion mining district of Attica, Greece, is one of the oldest mining areas of the world. In my master's thesis investigations on three minerals from this area are presented. The samples were especially studied by single-crystal X-ray diffraction as well as by infrared and Raman spectroscopy. The formula of guérinite $Ca_6(HAsO_4)_3(AsO_4)_2 \bullet 10.5H_2O$, was revised, based on a structure refinement in space group $P2_1/n$, with unit cell parameters a = 17.631 (2), b = 6.731 (1), c = 23.388 (3) Å, β = 90.69 (1)°, V = 2775.2 (6) $Å^3$, R1 = 0.051, wR2 = 0.094, Z = 4. Bismoclite BiOCl was analyzed in space group $P4/nmm$ with the following cell parameters a = 3.887 (2), c = 7.357 (5) Å, Z = 2, and V = 111.16 (14) $Å^3$, and refined to R1 = 0.013, wR2 = 0.036. Further, I contributed in the description of the new mineral tzeferisite $CaZn_8(SO_4)_2(OH)_{12}Cl_2 \bullet 9H_2O$; the results of the single-crystal X-ray diffractometry in space group $R\bar{3}c$ are a = 8.369 (12), c = 67.794 (14) Å, V = 4112.5 (14) $Å^3$, Z = 6, R1 = 0.036, wR2 = 0.089.

Abstract (deutsch)

Das Bergbaugebiet Lavrion in Attika, Griechenland, ist eines der ältesten Bergbaugebiete der Welt. In meiner Masterarbeit werden Untersuchungen an drei Mineralien aus diesem Gebiet vorgestellt. Die Proben wurden insbesondere durch Einkristall-Röntgenbeugung sowie durch Infrarot- und Raman-Spektroskopie untersucht. Die Formel von Guérinit $Ca_6(HAsO_4)_3(AsO_4)_2 \bullet 10.5H_2O$ wurde auf der Grundlage einer Strukturverfeinerung in der Raumgruppe $P2_1/n$ revidiert, mit den Einheitszellenparametern a = 17.631 (2), b = 6.731 (1), c = 23.388 (3) Å, β = 90.69 (1)°, V = 2775.2 (6) $Å^3$, R1 = 0.051, wR2 = 0.094, Z = 4. Bismoklit BiOCl wurde in der Raumgruppe $P4/nmm$ mit den folgenden Zellparametern a = 3,887 (2), c = 7,357 (5) Å, Z = 2 und V = 111,16 (14) $Å^3$ analysiert und verfeinert mit R1 = 0,013, wR2 = 0,036. Außerdem habe ich an der Beschreibung des neuen Minerals Tzeferisit $CaZn_8(SO_4)_2(OH)_{12}Cl_2 \bullet 9H_2O$ mitgewirkt; die Ergebnisse der Einkristall-Röntgendiffraktometrie in der Raumgruppe $R\bar{3}c$ sind a = 8,369 (12), c = 67,794 (14) Å, V = 4112,5 (14) Å3, Z = 6, R1 = 0,036, wR2 = 0,089.